Numerical study of bladed structures with geometric and contact nonlinearities

Elise Delhez, Florence Nyssen, Jean-Claude Golinval, Alain Batailly

POLYTECHNIQUE MONTRÉAL
UNIVERSITÉ D'INGÉNIERIE

LABORATOIRE D'ANALYSE VIBRATOIRE ET ACOUSTIQUE

Numerical study of bladed structures with geometric and contact nonlinearities

Elise Delhez[1,2], Florence Nyssen[1], Jean-Claude Golinval[2] Alain Batailly[1]

Abstract

This paper deals with the reduced order modeling of turbomachine bladed structures accounting for both geometric nonlinearities and nonlinear blade-tips/casing contacts in a numerically efficient way. A recently derived methodology, based on the concept of modal derivatives, is first used to study the contact interactions of a single rotating blade impacting a rigid casing. In this reduction procedure, nonlinear internal forces due to large displacements are evaluated using the stiffness evaluation procedure and contact is numerically handled with Lagrange multipliers. In-depth analyses, including clearance consumption computations and frequency analyses with a continuation procedure, are performed to understand and characterize the combined influence of contact and geometric nonlinearities on the blade's dynamics. The methodology is then generalized to full bladed disks using Component Mode Synthesis techniques with fixed interfaces. Each sector of the cyclically symmetric structure is projected onto a reduction basis composed of Craig–Bampton modes and a selection of their modal derivatives. A second reduction allows reducing the cyclic boundary degrees-of-freedom. The methodology is first assessed using a harmonic excitation at blade-tips, without contact. When applied to the bladed disk subjected to contact interactions, the methodology allows identifying the main interaction speeds that can be detrimental for the engine integrity. Through this work, the numerical strategy is applied on an open industrial compressor bladed disk model based on the NASA rotor 37 in order to promote the reproducibility of results.

Keywords

Reduced order modeling, Geometric nonlinearities, Rotor/stator interaction, Cyclic symmetry

1 - Départment de Génie Mécanique, Polytechnique Montréal, Montréal, (Québec) H3C 3A7, Canada.
2 - Département d'aérospatiale et mécanique, Université de Liège, allée de la Découverte 9, 4000 Liège, Belgique

Étude numérique de structures aubagées avec non-linéarités géométriques et contact

Elise Delhez[1,2], Florence Nyssen[1], Jean-Claude Golinval[2] Alain Batailly[1]

Résumé

Cet article porte sur la mise en place de modèles réduits de structures aubagées au sein des turbomachines en prenant en compte deux types de non-linéarités : des non-linéarités géométriques et des non-linéarités de type contact. Une méthode récemment publiée, reposant sur l'utilisation de dérivées modales, est tout d'abord utilisée pour l'analyse d'une aube seule subissant des contacts répétés avec le carter. Les forces internes non linéaires associées aux grands déplacements sont évaluées grâce à la méthode d'évaluation de la raideur (STEP pour *STiffness Evaluation Procedure*) et le contact est traité grâce à un calcul de multiplicateurs de Lagrange. Les analyses de quantités d'intérêt telles que la consommation de jeu et les analyses fréquentielles permettent de mieux comprendre et caractériser l'influence de chaque type de non-linéarité sur la réponse dynamique de l'aube. Une généralisation de la méthodologie est ensuite proposée pour permettre son application à des roues aubagées par le biais de méthodes de réduction à interfaces fixes. Chaque secteur de la roue aubagée, supposée à symétrie cyclique, est projeté sur un sous-espace engendré par une sélection de modes de Craig-Bampton et de leurs dérivées modales. Une seconde opération de réduction permet de condenser les frontières cycliques. Dans un premier temps, la méthodologie proposée est évaluée en considérant une excitation harmonique sur le sommet des aubes, sans contact. Puis, dans un second temps, l'application d'efforts de contact permet d'identifier les vitesses critiques de la roue aubagée. Tous les résultats présentés sont relatifs à un modèle ouvert d'aube de compresseur industriel : l'aube NASA rotor 37 afin de faciliter la reproductibilité des résultats.

Mots-clés

Réduction de modèle, Non-linéarités géométriques, Interactions rotor/stator, Symétrie cyclique

1 - Départment de Génie Mécanique, Polytechnique Montréal, Montréal, (Québec) H3C 3A7, Canada.
2 - Département d'aérospatiale et mécanique, Université de Liège, allée de la Découverte 9, 4000 Liège, Belgique

1 Introduction

Because of the new environmental regulations in aeronautics, engine manufacturers have to drastically reduce their environmental footprint. To achieve this, new engine architectures are being considered to improve the performance of turbojet engines and reduce their fuel consumption. Energy efficiency can be improved by controlling the clearance between the blade-tips and the stationary surrounding casing in order to reduce aerodynamic leaks. This strategy leads to more frequent occurrences of direct contacts between the rotating blades and the casing, even in nominal operating conditions. Moreover, the engine weight, and therefore the aircraft fuel consumption, can be reduced by designing lighter and slender blades. The use of these more flexible blades can lead to large displacements known as geometric nonlinear effects.

Because of the high costs associated to full-scale experimental setups, it is particularly important for manufacturers to have at their disposal accurate predictive numerical strategies [1]. However, as the use of thinner blades with reduced clearances with respect to the surrounding casing leads to large amplitudes of vibration and contact occurrences, classical linear models become inaccurate. New numerical tools allowing to account for these nonlinear structural considerations from the beginning of the design process are thus needed.

Turbomachine bladed structures are generally modeled by 3D finite element models with high fidelity geometrical details and material distribution. Current industrial numerical models of bladed structures are therefore characterized by a very large number of degrees-of-freedom and their direct use in dynamic analysis requires high computational capabilities. This is particularly true in a nonlinear context. This is the reason why many recent works are devoted to the construction of nonlinear reduced order models that can be used to reduce the computational burden in a design process, but also as fast executing replacements of the full order model or to extract relevant information hidden in the full order model. There exists different categories of reduction methods, from goal-oriented reduction approaches to physical reduction methods [2]. Among the existing physical reduction methods, projection on a reduced space is widely used in the literature because of its ease of implementation, but also because it preserves the general expression of the equation of motion so that the same time integration algorithms as those used for the full order model can be used.

In a linear context, the dynamics of cyclically symmetric structures is generally studied in the harmonic space where the dynamic problem can be written as a set of sub-problems for each harmonic using Fourier formalism [3, 4, 5]. This cyclic symmetry formulation can be used in classical linear reduced order modeling techniques (such as Craig-Bampton or Craig-Martinez reduction methods [6, 7, 8]) to efficiently compute the reduction basis [9]. Combined with penalty methods [10] or Lagrange multiplier approaches [11], these reduction methods have proven to provide accurate prediction of contact dynamics, and in particular of rubbing events between blades and casings [12].

When geometric nonlinearities are considered or in the case of severe contact nonlinearities, the response of the structure can no longer be expressed with independent diameters as the nonlinearities induce a coupling between the harmonic components. The cyclic symmetry formulation can no longer be used. In this context, different projective reduction methods have been developed. They can be grouped in two categories: reduction methods for which the structure is reduced as a whole and reduction methods where the structure is divided into individual sectors. On the one hand, for simple structures, the equations of motion of the full finite element model of the cyclically symmetric structure can be directly projected onto a reduced space with a reduction basis intrinsically accounting for the nonlinear behavior of the structure based on modal derivatives [13, 14] or on Proper Orthogonal Decomposition [15, 16] for instance. For more complex industrial structures, this reduction can be preceded by a first projection such as a modal reduction [15]. On the other hand, some reduction methods are based on Component Mode Synthesis [17, 18]: the structure's dynamics is described by a set of modes of the individual sectors and interface (or constraint) modes that allow to account for the coupling between the sectors. Different definitions of the sector modes have been investigated in a nonlinear context such as linear modes augmented with modal derivatives [19, 20] or nonlinear normal modes [21, 22].

In these reduced order modeling techniques, nonlinear forces due to large displacements are identified either with intrusive or non-intrusive methods. In intrusive methods, reduced nonlinear forces are obtained by direct projection of the full order nonlinear force [23, 24, 25, 15] based on the relationship between the finite element tensors and their modal counterparts. In non-intrusive methods, the reduced nonlinear forces are expressed as a polynomial form of the reduced coordinates whose coefficients are identified with nonlinear static evaluations with imposed

displacements (enforced displacement method or STiffness Evaluation Procedure (STEP) [26]) or imposed forces (applied force method [27]).

A methodology has been recently derived to study the contact interactions of a single blade undergoing large displacements [28]. This methodology is based on non-intrusive projection-based reduction techniques in order to be compatible with commercial finite element software packages, with computations made in the time domain in order to capture transient phenomena which are key for the rise of some critical interactions [29]. This article serves two main objectives. First, deeper analyses are performed with the single-sector methodology in order to complete the analyses done in the first paper where the methodology has been presented [28] and better understand and quantify the influence of geometric nonlinearities in contact dynamics. Then, this paper aims at generalizing the methodology to cyclically symmetric bladed disks using Component Mode Synthesis techniques with fixed interfaces. The second objective of this paper is to show that reduced order modeling techniques offer a computationally efficient alternative to full finite element models to study the nonlinear dynamics of such structures.

The paper is divided into two main parts. Section 2 is dedicated to single-sector structures. First, the existing reduction methodology is briefly recalled. The methodology is then applied to a single blade periodically impacting a rigid surrounding casing. In-depth analyses, including clearance consumption computations and the use of a continuation procedure to obtain nonlinear frequency response curves, are performed to understand and characterize the influence of geometric nonlinearities. Full bladed disks are then studied in section 3. The proposed methodology is generalized for full bladed disks and validated on a test case subjected to an equivalent aerodynamic loading, without contact interactions. The influence of the number of modal derivatives included in the reduction basis and of how they are selected is discussed. Lastly, the methodology is used to study contact interactions of a full bladed disk.

2 Single blade analysis

Single-blade structures are here studied with the reduction methodology developed and validated in [28, 30]. This methodology is first briefly recalled in section 2.1 along with some additional numerical considerations regarding the computation of the internal nonlinear forces. Then, a specific case study is presented in section 2.2 with a description of the open blade model selected as well as the considered contact scenario. Results of contact simulations are presented in section 2.3 with in-depth analyses regarding clearance consumption and contact stiffening.

2.1 Methodology

Considering a high-fidelity finite element model of a mechanical bladed structure with N_{DOF} degrees-of-freedom, the spatially discretized equation of motion governing the physical displacement $\mathbf{u}$ of the structure around its equilibrium state writes

$$\mathbf{M}\ddot{\mathbf{u}} + \mathbf{C}\dot{\mathbf{u}} + \mathbf{K}\mathbf{u} + \mathbf{g}_{\text{nl}}(\mathbf{u}) = \mathbf{f}_e(t) + \mathbf{f}_c(\mathbf{u}, \dot{\mathbf{u}}), \tag{1}$$

where $\mathbf{M}$ is the mass matrix, $\mathbf{C}$ is the viscous damping matrix, $\mathbf{K}$ is the linear stiffness matrix, $\mathbf{g}_{\text{nl}}(\mathbf{u})$ is the nonlinear internal forces vector due to large displacements, $\mathbf{f}_e(t)$ is the external forces vector and $\mathbf{f}_c(\mathbf{u}, \dot{\mathbf{u}})$ accounts for possible contact interactions. The time dependence of $\mathbf{u}$ is omitted for clarity.

In this work, finite element models are reduced using linear projection-based model order reduction techniques, *i.e.* the displacement field $\mathbf{u}$ is written as a linear combination of spatial basis functions $\mathbf{\Phi}$ as

$$\mathbf{u}(t) = \mathbf{\Phi}\,\mathbf{q}(t) = \sum_{j=1}^{r} \boldsymbol{\phi}_j q_j(t) \tag{2}$$

and the physical displacement $\mathbf{u} \in \mathbb{R}^{N_{\text{DOF}}}$ is linearly reduced to a set of generalized coordinates $\mathbf{q} \in \mathbb{R}^r$, where $r \leqslant N_{\text{DOF}}$ (in practice $r \ll N_{\text{DOF}}$). Injecting Eq. (2) in Eq. (1), the projection of the equation of motion in the reduced space writes

$$\tilde{\mathbf{M}}\ddot{\mathbf{q}} + \tilde{\mathbf{C}}\dot{\mathbf{q}} + \tilde{\mathbf{K}}\mathbf{q} + \tilde{\mathbf{g}}_{\text{nl}}(\mathbf{q}) = \tilde{\mathbf{f}}_e(t) + \tilde{\mathbf{f}}_c(\mathbf{q}, \dot{\mathbf{q}}), \tag{3}$$

where the projected matrices take the expressions

$$\tilde{\mathbf{M}} = \mathbf{\Phi}^{\mathrm{T}}\mathbf{M}\mathbf{\Phi}, \qquad \tilde{\mathbf{C}} = \mathbf{\Phi}^{\mathrm{T}}\mathbf{C}\mathbf{\Phi}, \qquad \tilde{\mathbf{K}} = \mathbf{\Phi}^{\mathrm{T}}\mathbf{K}\mathbf{\Phi} \tag{4}$$

and the projected vectors are

$$\tilde{\mathbf{g}}_{\mathrm{nl}}(\mathbf{q}) = \mathbf{\Phi}^{\mathrm{T}}\mathbf{g}_{\mathrm{nl}}(\mathbf{u}), \qquad \tilde{\mathbf{f}}_e = \mathbf{\Phi}^{\mathrm{T}}\mathbf{f}_e, \qquad \tilde{\mathbf{f}}_c(\mathbf{q},\dot{\mathbf{q}}) = \mathbf{\Phi}^{\mathrm{T}}\mathbf{f}_c(\mathbf{u},\dot{\mathbf{u}}). \tag{5}$$

This way of reducing a mechanical system advantageously preserves the general form of the equation of motion. In this nonlinear context, projection-based reduction methods are characterized by (1) the definition of the reduction basis $\mathbf{\Phi}$ and (2) how the nonlinear forces due to large displacements and contact interactions are evaluated in the reduced space.

The physical displacement vector $\mathbf{u}$ is partitioned into inner degrees-of-freedom, $\mathbf{u}_i$, that are effectively reduced, and boundary degrees-of-freedom, $\mathbf{u}_b$, that are kept as physical degrees-of-freedom in the reduced space as

$$\mathbf{u} = \begin{bmatrix} \mathbf{u}_i \\ \mathbf{u}_b \end{bmatrix}. \tag{6}$$

Structural matrices $\mathbf{M}$, $\mathbf{C}$ and $\mathbf{K}$ and force vectors $\mathbf{g}_{\mathrm{nl}}$, $\mathbf{f}_e$ and $\mathbf{f}_c$ are partitioned accordingly with respect to inner (subscript i) and boundary (subscript b) degrees-of-freedom. The vector of generalized coordinates $\mathbf{q}$ can therefore be written as

$$\mathbf{q} = \begin{bmatrix} \mathbf{u}_b \\ \boldsymbol{\eta} \end{bmatrix}, \tag{7}$$

where $\boldsymbol{\eta}$ stands for modal generalized coordinates. As shown further, the boundary degrees-of-freedom $\mathbf{u}_b$ are here chosen as blade-tips degrees-of-freedom where contact events may occur. This allows the treatment of contact directly in the reduced space.

2.1.1 Reduction basis

In this work, the reduction basis $\mathbf{\Phi}$ is composed of r Craig-Bampton modes [18] and a selection of r_{MD} modal derivatives [31, 32]. The Craig-Bampton modes consist in r_b constraint modes $\mathbf{\Psi}$ and r_c fixed interface linear normal modes $\mathbf{\Theta}$.

The constraint modes are defined as the static modes resulting from imposed unit displacements on the boundary degrees-of-freedom $\mathbf{u}_b$. Adopting the degrees-of-freedom partitioning described above, they can be written as

$$\mathbf{\Psi} = \begin{bmatrix} \mathbf{\Psi}_i \\ \mathbf{I} \end{bmatrix}, \tag{8}$$

where

$$\mathbf{\Psi}_i = -\mathbf{K}_{ii}^{-1}\mathbf{K}_{ib}. \tag{9}$$

The fixed interface linear normal modes correspond to the modes of the structure clamped at the boundary interface degrees-of-freedom $\mathbf{u}_b$. They can be written as

$$\mathbf{\Theta} = \begin{bmatrix} \mathbf{\Theta}_{i,r_c} \\ \mathbf{0} \end{bmatrix}, \tag{10}$$

where $\mathbf{\Theta}_{i,r_c}$ is formed by truncating the solution $\mathbf{\Theta}_i$ of the eigenvalue problem

$$\mathbf{K}_{ii}\mathbf{\Theta}_i = \mathbf{M}_{ii}\mathbf{\Theta}_i\mathbf{\Omega}^2 \tag{11}$$

to the first r_c modes.

In order to account for the second-order effects that occur when considering geometric nonlinearities, the Craig-Bampton basis is enriched with modal derivatives (MD). The modal derivatives, first introduced by Idelsohn and Cardona [33], are here derived from the static problem [32]

$$\mathbf{K}\mathbf{u} + \mathbf{g}_{\text{nl}}(\mathbf{u}) = \mathbf{f}_e, \tag{12}$$

where the imposed static load writes

$$\mathbf{f}_e = \mathbf{K} \sum_{j=1}^{r_b+r_c} \breve{\boldsymbol{\phi}}_j \breve{\eta}_j, \tag{13}$$

where $\breve{\boldsymbol{\phi}}_j$ stands for the j^{th} Craig-Bampton mode and $\breve{\eta}_j$ is the j^{th} Craig-Bampton generalized coordinate. The displacement $\mathbf{u}$ can be expanded in Taylor series around the equilibrium position $\breve{\boldsymbol{\eta}} = \mathbf{0}$ as

$$\mathbf{u} = \sum_{j=1}^{r_b+r_c} \left.\frac{\partial \mathbf{u}}{\partial \breve{\eta}_j}\right|_{\breve{\boldsymbol{\eta}}=\mathbf{0}} \breve{\eta}_j + \frac{1}{2} \sum_{j=1}^{r_b+r_c} \sum_{k=1}^{r_b+r_c} \left.\frac{\partial^2 \mathbf{u}}{\partial \breve{\eta}_j \partial \breve{\eta}_k}\right|_{\breve{\boldsymbol{\eta}}=\mathbf{0}} \breve{\eta}_j \breve{\eta}_k + \cdots . \tag{14}$$

The derivatives of the displacement vector with respect to the generalized coordinates can be computed by differentiating the static problem (12). Differentiating Eq. (12) and evaluating this expression at the equilibrium position gives

$$\left.\frac{\partial \mathbf{u}}{\partial \breve{\eta}_j}\right|_{\breve{\boldsymbol{\eta}}=\mathbf{0}} = \breve{\boldsymbol{\phi}}_j \qquad j = 1, \cdots, r_b + r_c. \tag{15}$$

These derivatives correspond to the linear Craig-Bampton modes. The second order derivatives of the displacement vector are defined as the modal derivatives

$$\boldsymbol{\xi}_{jk} = \left.\frac{\partial^2 \mathbf{u}}{\partial \breve{\eta}_j \partial \breve{\eta}_k}\right|_{\breve{\boldsymbol{\eta}}=\mathbf{0}} \qquad j,\, k = 1, \cdots, r_b + r_c. \tag{16}$$

They are computed by differentiating two times Eq. (12) and evaluating the resulting expression at the equilibrium position. The modal derivatives are therefore computed by solving the linear systems

$$\mathbf{K}\boldsymbol{\xi}_{jk} = -\left.\frac{\partial \mathbf{K}_T}{\partial \breve{\eta}_k}\right|_{\breve{\boldsymbol{\eta}}=\mathbf{0}} \breve{\boldsymbol{\phi}}_j, \tag{17}$$

where the tangent stiffness matrix is defined as

$$\mathbf{K}_T = \mathbf{K} + \frac{\partial \mathbf{g}_{\text{nl}}}{\partial \mathbf{u}}. \tag{18}$$

In the case where the finite element package provides the tangent stiffness matrix, the derivative of the tangent stiffness matrix can be computed by finite differences as

$$\left.\frac{\partial \mathbf{K}_T}{\partial \breve{\eta}_k}\right|_{\breve{\boldsymbol{\eta}}=\mathbf{0}} = \frac{\mathbf{K}_T\left(\epsilon_k \breve{\boldsymbol{\phi}}_k\right) - \mathbf{K}}{\epsilon_k}, \tag{19}$$

where the coefficients ϵ_k should be carefully defined. The right-hand side of Eq. (17) can also be written in terms of the second derivative of the nonlinear internal forces, which can be useful to evaluate the modal derivatives in the case where the finite element package only outputs the reaction forces due to nonlinear static displacements.

The interface component of the modal derivatives is not null since the interface is not set fixed. Since the interface motion is already fully represented by the constraint modes, the modal derivatives are modified to fixed interface modes by subtracting the component already present in the constraint modes

$$\begin{bmatrix} \boldsymbol{\zeta}_{jk} \\ \mathbf{0} \end{bmatrix} = \begin{bmatrix} \boldsymbol{\xi}_{jk,i} \\ \boldsymbol{\xi}_{jk,b} \end{bmatrix} - \begin{bmatrix} \boldsymbol{\Psi}_i \\ \mathbf{I} \end{bmatrix} \boldsymbol{\xi}_{jk,b}. \tag{20}$$

It can be shown that modal derivatives are symmetric [34], *i.e.*

$$\boldsymbol{\zeta}_{jk} = \boldsymbol{\zeta}_{kj}, \tag{21}$$

so that a basis consisting in r linear modes can be enhanced with $r(r+1)/2$ modal derivatives.

The augmented Craig-Bampton reduction basis and the associated reduction technique therefore write

$$\mathbf{u} = \boldsymbol{\Phi}\mathbf{q} = \begin{bmatrix} \boldsymbol{\Psi}_i & \boldsymbol{\Theta}_{i,r_c} & \mathbf{Z} \\ \mathbf{I} & \mathbf{0} & \mathbf{0} \end{bmatrix} \begin{bmatrix} \mathbf{u}_b \\ \boldsymbol{\eta}_c \\ \boldsymbol{\eta}_{\mathrm{MD}} \end{bmatrix}, \tag{22}$$

where the modal derivatives $\boldsymbol{\zeta}_{jk}$ are combined in $\mathbf{Z}$ and $\boldsymbol{\eta}_c$ and $\boldsymbol{\eta}_{\mathrm{MD}}$ are modal generalized coordinates corresponding to the fixed interface linear normal modes and the fixed interface modal derivatives. In practice, only a selection of modal derivatives are included in the reduction basis to capture the nonlinear behavior of the structure. A modal derivatives subset is therefore selected as done in previous works [28]. In practice, a weight W_{jk} is associated to each modal derivative and the modal derivatives with the highest weights are included in the reduction basis. Further investigations regarding modal derivatives selection will be carried out when generalizing the methodology to full bladed disks in section 3.1.

2.1.2 Reduced nonlinear internal forces

The reduced nonlinear internal forces are evaluated with the STEP, introduced in [26]. In the STEP, the nonlinear reduced term is assumed to be polynomial of degree 3 in terms of the generalized coordinates $q_1, q_2, \ldots, q_r$, components of the vector of generalized coordinates $\mathbf{q}$. The degree of this polynomial reflects the fact that the nonlinearities in the nonlinear internal forces $\mathbf{g}_{\mathrm{nl}}(\mathbf{u})$ are cubic for some elements types. In particular, it is an exact expansion in the case of 3D finite element elements under the assumption of a linearly elastic material or for beam, plate and shell finite elements based on von Kármán strain/displacement law, whereas it is truncated for corotational elements [24, 35, 36]. The polynomial formulation reads

$$\tilde{\mathbf{g}}_{\mathrm{nl}}(\mathbf{q}) = \widetilde{\boldsymbol{\mathcal{A}}}(\mathbf{q},\mathbf{q}) + \widetilde{\boldsymbol{\mathcal{B}}}(\mathbf{q},\mathbf{q},\mathbf{q}), \tag{23}$$

using the functional notation $\widetilde{\boldsymbol{\mathcal{A}}}(\cdot,\cdot)$ and $\widetilde{\boldsymbol{\mathcal{B}}}(\cdot,\cdot,\cdot)$ for the quadratic and cubic terms with coefficients gathered in the third-order tensor[1] $\tilde{\mathbf{A}}$ and the fourth-order tensor $\tilde{\mathbf{B}}$. The explicit indicial expression of the nonlinear internal forces writes

$$\tilde{g}^m_{\mathrm{nl}}(\mathbf{q}) = \sum_{i=1}^{r}\sum_{j=i}^{r} \tilde{A}^m_{ij}\, q_i q_j + \sum_{i=1}^{r}\sum_{j=i}^{r}\sum_{k=j}^{r} \tilde{B}^m_{ijk}\, q_i q_j q_k, \tag{24}$$

with $m = 1, 2, \ldots, r$. The coefficients $\tilde{A}^m_{ij}$ and $\tilde{B}^m_{ijk}$ of tensors $\tilde{\mathbf{A}}$ and $\tilde{\mathbf{B}}$ are determined by nonlinear forces static evaluations performed on the full order finite element model. The procedure is not recalled here for the sake of conciseness but is detailed in [28].

[1] The term 'tensor' used here simply refers to a multidimensional array of dimension larger than 2.

2.1.3 Contact treatment

Contact is here numerically treated in the reduced space using Lagrange multipliers, with a prediction/correction scheme. The numerical strategy relies on the explicit central difference time integration scheme and is known as the Lagrange forward multiplier algorithm [11]. Simulating the response of the system in the time domain allows capturing its transient dynamics following contact events. Friction is managed with the Coulomb law, under the assumption of sliding friction as the tangential speed to rotation is significantly larger than the vibration speed of the structure.

By noting $\mathbf{q}_n$, the numerical approximation of the exact value $\mathbf{q}(t_n)$, the classical explicit central finite difference scheme used in this work yields

$$\ddot{\mathbf{q}}_n = \frac{\mathbf{q}_{n+1} - 2\mathbf{q}_n + \mathbf{q}_{n-1}}{h^2} \quad \text{and} \quad \dot{\mathbf{q}}_n = \frac{\mathbf{q}_{n+1} - \mathbf{q}_{n-1}}{2h}, \tag{25}$$

where h is the time step of integration. At each time step $t_{n+1} = t_n + h$, the displacement field is first predicted without accounting for possible contact interaction as

$$\begin{aligned} \mathbf{q}^\star_{n+1} = &\left(2\tilde{\mathbf{M}} + h\tilde{\mathbf{C}}\right)^{-1} \left\{2h^2 \left[\tilde{\mathbf{f}}_e(t_n) - \tilde{\mathbf{g}}_{\text{nl}}(\mathbf{q}_n)\right]\right. \\ &\left. + \left(4\tilde{\mathbf{M}} - 2h^2\tilde{\mathbf{K}}\right)\mathbf{q}_n + \left(h\tilde{\mathbf{C}} - 2\tilde{\mathbf{M}}\right)\mathbf{q}_{n-1}\right\}. \end{aligned} \tag{26}$$

Based on the predicted displacements, the gap between the blade and the casing is then evaluated at the blade-tip nodes whose degrees-of-freedom are kept among the generalized coordinates. If penetrations are detected, *i.e.* if any gap becomes negative, contact forces $\tilde{\mathbf{f}}_{c,n+1}$ are computed in the normal and tangential directions through the use of Lagrange multipliers using the methodology described in [11] in order to cancel out the penetrations of the impacting nodes. The contact forces are then used to correct the non-admissible displacements by

$$\mathbf{q}_{n+1} = \mathbf{q}^\star_{n+1} + \left(\frac{\tilde{\mathbf{M}}}{h^2} + \frac{\tilde{\mathbf{C}}}{2h}\right)^{-1} \tilde{\mathbf{f}}_{c,n+1}. \tag{27}$$

The treatment of contact in the reduced space with Lagrange multipliers (without geometric nonlinearities) has been validated against full order model data [37] and experimental data [38, 39].

2.1.4 Efficient implementation of nonlinear forces computation

Previous studies performed with the single-blade methodology show that it is necessary to include a sufficiently high number of modal derivatives in the reduction basis to correctly capture the behavior of geometrically nonlinear blades subjected to contact interactions as contact events may excite high-frequency modes [30, 28]. In practice, around $r = 150$ modes are required to accurately describe the dynamics of typical single-sector structures. With such reduction bases, the evaluation of the nonlinear internal forces with Eq. (23) can become computationally expensive as the size of the tensor $\tilde{\mathbf{B}}$ increases with the fourth power of r.

The contact algorithm described in section 2.1.3 takes the form of a time loop with a succession of matrix/vector products. Previous studies performed with this algorithm based on Lagrange multipliers show that a time step of integration of the order of 10^{-7} second (corresponding to approximately 0.01% of the period of the first bending mode of the blade) has to be considered. At each time step, the nonlinear forces are evaluated in the prediction step given by Eq. (26). The prediction step of the contact algorithm can be re-written as

$$\mathbf{q}^\star_{n+1} = \mathbf{X}_0\tilde{\mathbf{f}}_e(t_n) + \mathbf{X}_1\mathbf{q}_n + \mathbf{X}_2\mathbf{q}_{n-1} + \boldsymbol{\mathcal{X}}_3(\mathbf{q}_n, \mathbf{q}_n) + \boldsymbol{\mathcal{X}}_4(\mathbf{q}_n, \mathbf{q}_n, \mathbf{q}_n) \tag{28}$$

where $\mathbf{q}^\star_{n+1}$ is the prediction of the displacement at time t_{n+1}, $\tilde{\mathbf{f}}_e$ is the reduced external force, $\mathbf{q}_n$ and $\mathbf{q}_{n-1}$ are the displacements computed at time t_n and t_{n-1} and where

$$\mathbf{X}_0 = 2h^2\left(2\tilde{\mathbf{M}} + h\tilde{\mathbf{C}}\right)^{-1}, \tag{29}$$

$$\mathbf{X}_1 = \left(2\tilde{\mathbf{M}} + h\tilde{\mathbf{C}}\right)^{-1}\left(4\tilde{\mathbf{M}} - 2h^2\tilde{\mathbf{K}}\right), \tag{30}$$

$$\mathbf{X}_2 = \left(2\tilde{\mathbf{M}} + h\tilde{\mathbf{C}}\right)^{-1}\left(h\tilde{\mathbf{C}} - 2\tilde{\mathbf{M}}\right), \tag{31}$$

$$\boldsymbol{\mathcal{X}}_3(\cdot,\cdot) = -2h^2\left(2\tilde{\mathbf{M}} + h\tilde{\mathbf{C}}\right)^{-1}\tilde{\boldsymbol{\mathcal{A}}}\,(\cdot,\cdot), \tag{32}$$

and

$$\boldsymbol{\mathcal{X}}_4(\cdot,\cdot,\cdot) = -2h^2\left(2\tilde{\mathbf{M}} + h\tilde{\mathbf{C}}\right)^{-1}\tilde{\boldsymbol{\mathcal{B}}}\,(\cdot,\cdot,\cdot). \tag{33}$$

Coefficients of functional forms $\boldsymbol{\mathcal{X}}_3(\cdot,\cdot)$ and $\boldsymbol{\mathcal{X}}_4(\cdot,\cdot,\cdot)$ are gathered in the third-order tensor $\mathbf{X}_3$ and the fourth-order tensor $\mathbf{X}_4$. Matrices and tensors $\mathbf{X}_i$ $(i = 0,\ldots,4)$ are constant and can be computed once at the beginning of the simulation.

At each time step, the matrices and tensors $\mathbf{X}_i$ $(i = 0,\ldots,4)$ are transferred from the memory to the processor, they are respectively multiplied by $\tilde{\mathbf{f}}_e(t_n)$, $\mathbf{q}_n$, $\mathbf{q}_{n-1}$ and used in the nonlinear functions (that can be seen as 'tensors products'), and the resulting quantities are summed up. These two steps (transfer from RAM and mathematical operations) have to be considered when optimizing the code to reduce computation times. In practice, on powerful computation servers, computations are often limited by the DRAM bandwidth, more than by the number of operations that can be done per second. In the matrix/vector products in Eq. (28), each element of the matrices is used only once in the multiplications, which is not very profitable. We therefore realize several simulations together, going forward in time for each simulation at the same time. Provided the matrices and tensors $\mathbf{X}_i$ $(i = 0,\ldots,4)$ are the same for each simulation, the prediction step of the contact algorithm given by Eq. (28) can be re-written as

$$\mathbf{Q}^{\star}_{n+1} = \mathbf{X}_0\tilde{\mathbf{F}}_e(t_n) + \mathbf{X}_1\mathbf{Q}_n + \mathbf{X}_2\mathbf{Q}_{n-1} + \boldsymbol{\mathcal{X}}_3\left(\mathbf{Q}_n,\mathbf{Q}_n\right) + \boldsymbol{\mathcal{X}}_4\left(\mathbf{Q}_n,\mathbf{Q}_n,\mathbf{Q}_n\right), \tag{34}$$

where the matrices $\mathbf{Q}^{\star}_{n+1}$, $\tilde{\mathbf{F}}_e$, $\mathbf{Q}_n$ and $\mathbf{Q}_{n-1}$ are respectively the concatenations of the vectors $\mathbf{q}^{\star}_{n+1}$, $\tilde{\mathbf{f}}_e$, $\mathbf{q}_n$ and $\mathbf{q}_{n-1}$ related to each simulation and where

$$\left[\boldsymbol{\mathcal{X}}_3\left(\mathbf{Q}_n,\mathbf{Q}_n\right)\right](m,p) = \sum_{i=1}^{r}\sum_{j=i}^{r}\mathbf{X}_3\left(m,i,j\right)\mathbf{Q}_n\left(i,p\right)\mathbf{Q}_n\left(j,p\right) \tag{35}$$

and

$$\left[\boldsymbol{\mathcal{X}}_4\left(\mathbf{Q}_n,\mathbf{Q}_n,\mathbf{Q}_n\right)\right](m,p) = \sum_{i=1}^{r}\sum_{j=i}^{r}\sum_{k=j}^{r}\mathbf{X}_4\left(m,i,j,k\right)\mathbf{Q}_n\left(i,p\right)\mathbf{Q}_n\left(j,p\right)\mathbf{Q}_n\left(k,p\right). \tag{36}$$

This way, the matrix/vector products are replaced by matrix/matrix products where the elements of the matrices loaded from the memory are used more than one time, which is more profitable and can theoretically accelerate the computations. As $\mathbf{X}_i$ $(i = 0,\ldots,4)$ only depend on the time step of integration and the structural matrices, the different simulations performed together can be characterized by different contact conditions (friction coefficient, clearance value...) or different angular speeds. This can be particularly beneficial to build interaction maps as it requires to perform contact simulations on a wide range of angular speeds. Note that this numerical strategy that consists in evaluating several vectors of nonlinear internal forces at the same time can also be used to compute the nonlinear internal forces of tuned multi-sector structures under the assumption of linear coupling between the sectors that is made here.

The products $\mathbf{X}_0\tilde{\mathbf{F}}_e(t_n)$, $\mathbf{X}_1\mathbf{Q}_n$ and $\mathbf{X}_2\mathbf{Q}_{n-1}$ in Eq. (34) are products of 2D matrices that can be computed easily. By contrast, the functional forms $\boldsymbol{\mathcal{X}}_3(\mathbf{Q}_n, \mathbf{Q}_n)$ and $\boldsymbol{\mathcal{X}}_4(\mathbf{Q}_n, \mathbf{Q}_n, \mathbf{Q}_n)$ are kinds of products of 3D tensors and 4D tensors whose computation has to be optimized to avoid loosing the benefit of the numerical strategy. In order to remove useless monomials redundancy in the products, the tensors $\mathbf{X}_3$ and $\mathbf{X}_4$ are first transformed to 'upper triangular' or 'upper pyramidal' tensors, *i.e.* $\mathbf{X}_3(m,i,j) = 0$ except for $i < j$ and $\mathbf{X}_4(m,i,j,k) = 0$ except for $i < j < k$. An adapted tensor multiplication function, accounting for the particular structure of tensors $\mathbf{X}_3$ and $\mathbf{X}_4$, has been implemented on top of the BLIS framework to perform efficiently the products [40]. The multi-threaded implementation is inspired from the BLIS implementation of the product of triangular matrices [41].

This numerical strategy allows considerably reducing computation times (by a factor between 5 and 15, depending on the processor). For instance, contact simulations at 80 different angular speeds (for given contact conditions and reduced order model) took 20 hours on 8 cores with this numerical strategy with memory sharing against 200 hours in the same conditions on the same machine without proper memory reuse.

2.2 Case study

While obtaining relevant results for industrial mechanical systems calls for the use of realistic full 3D finite element models, the latter often prevent full disclosure of the results for confidentiality reasons. It is thus extremely arduous to compare existing numerical strategies dedicated to such analyses. The reduction procedure is here applied on an open industrial compressor blade model in order to promote reproducibility of results. The next two sections describe the blade model used throughout this article and the contact scenario to initiate contact interactions between the blade and the surrounding casing together with the parameters of the numerical simulations.

2.2.1 Blade model

In this paper, the methodology is applied to an industrial blade model based on the NASA rotor 37 [2]. NASA rotor 37 is a transonic axial flow compressor stage composed of 36 blades (see Fig. 1). It was initially designed and tested at NASA's Lewis Research Center in the late 70's as part of aerodynamic research [42, 43]. Since then, NASA rotor 37 has been often used as a benchmark to validate numerical methods and assess the performance of numerical solvers in the fields of computational fluid dynamics [44] and, more recently, in structural dynamics [45, 46, 47, 48]. Its open geometry easily allows methods validation, results reproducibility and works comparison.

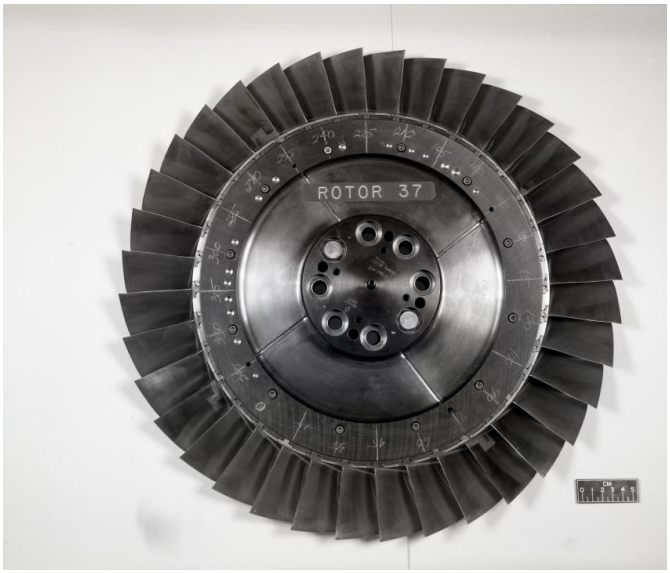

Figure 1. Picture of NASA rotor 37 [49].

[2]The CAD file and the finite element model are available at https://gitlab.lava.polymtl.ca/depots_publics/modeles/rotor37.

Rotor 37 is made of 200-grade maraging steel, a nickel alloy [43], with Young's modulus $E = 180$ GPa, Poisson's ratio $\nu = 0.3$, density $\rho = 8,000$ kg/m^3 and yield stress $\sigma_Y = 1.38$ GPa. The blade 3D geometry is described with a finite element model composed of quadratic pentahedral elements as shown in Fig. 2. The discretized mesh of the blade is represented in Fig. 2. It counts 20,657 nodes, *i.e.* 61,971 degrees-of-freedom. The compressor blade is clamped at its root. The first three eigenfrequencies of the blades are given by $\omega_1 = 5,272$ rad/s, $\omega_2 = 15,760$ rad/s and $\omega_3 = 19,071$ rad/s. They correspond respectively to the first bending (1B), first torsion (1T) and second bending (2B) modes. The damping matrix $\mathbf{C}$ is computed in the modal domain. Modal damping coefficients $\xi_{1-3} = 5 \cdot 10^{-4}$ for the first three modes and $\xi_{4+} = 5 \cdot 10^{-3}$ for the higher frequency modes are considered in the whole study in agreement with previous studies performed on the same structure [47].

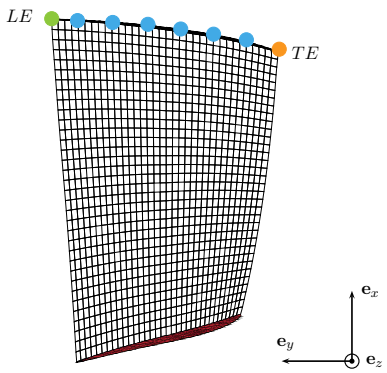

Figure 2. Single blade of NASA rotor 37 with mesh used for the finite element simulations and clamped surface (■). The eight colored nodes are the blade tip nodes retained for contact simulations. Among those nodes, the node TE is located at the trailing edge (●) and the node LE is located at the leading edge (●) (from [28]).

2.2.2 Contact scenario

The bladed disk is assumed to rotate at a constant speed Ω about the $\mathbf{e}_z$ axis (period of revolution $T = 2\pi/\Omega$). The structure is surrounded by a casing assumed to be infinitely rigid, *i.e.* insensitive to blade contact events. The casing follows the shape of the blade tip, so that the clearance c_0 between the blade (at rest) and the casing is uniform from the leading edge (node LE) to the trailing edge (node TE), see Fig. 3.

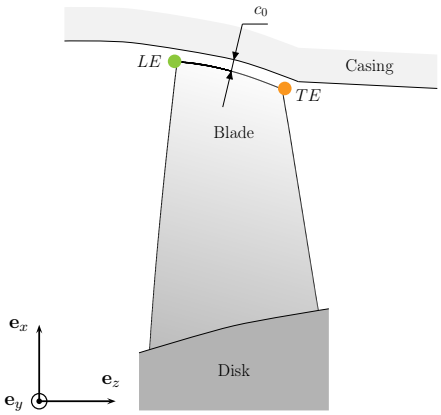

Figure 3. Cut view of the NASA rotor 37 blade surrounded by the casing and clamped on the disk (from [28]).

At the beginning of the simulation, the casing is perfectly circular to avoid any initial penetration, with an operating clearance between the blade tip nodes and the circular casing c_0. In order to initiate contact, the casing is

then progressively deformed in the radial direction until reaching its final distortion

$$f(\theta) = (c_0 + p_0) \exp\left[-\left(\frac{\theta - \lfloor \theta/\pi \rfloor \pi - \pi/2}{0.15}\right)^2\right], \tag{37}$$

where θ is the angular coordinate varying between 0 and 2π and p_0 defines the penetration of the casing profile (- - -) with respect to the circular trajectory (- - -) of a blade-tip node (●) of the sector at rest as shown in Fig. 4. This distortion corresponds to an ovalization of the casing with the creation of two diametrically opposed bumps of height $h_b = c_0 + p_0$ corresponding to privileged contact areas (see Fig. 4). The gap between a given blade tip node and the casing is therefore computed through

$$g(\theta_b, t) = c_0 - (1 - e^{-\alpha t}) f(\theta_b) - u_r(t), \tag{38}$$

where θ_b is the current angular position of the blade tip node, u_r is the radial displacement of the considered node and α is defined such that the ovalization reaches 99% of the maximal distortion at 20% of the total simulation time.

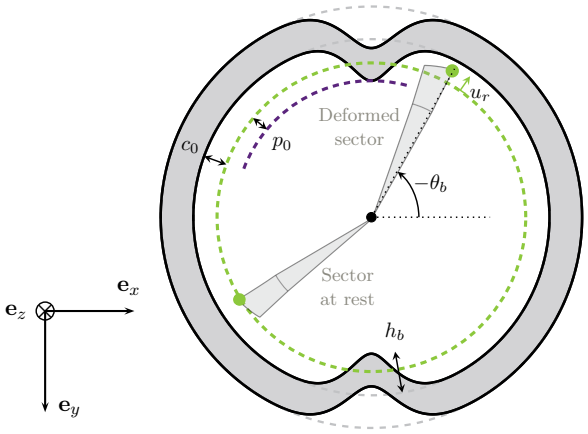

Figure 4. Ovalization of the casing from (⌜⌝) to (□), penetration of the casing profile (- - -) with respect to the circular trajectory (- - -) of a blade-tip node (●) of the sector at rest and definition of the parameters in Eq. (38) for the gap computation (not to scale).

The degrees-of-freedom of the 8 boundary nodes colored in Fig. 2 distributed between the nodes LE and TE are kept in the reduced space and define the contact interface. When applied to the whole multi-sector structure, the degrees-of-freedom of the 8 boundary nodes of each blade are kept in the reduction basis. Possible penetrations and contact forces are computed at these nodes only.

In the following, the clearance c_0 is set to 0.5 mm, and the height of bumps is defined as $h_b = 0.625$ mm. As detailed in section 2.1.3, contact is numerically handled with Lagrange multipliers and the equation of motion is integrated forward in time using an explicit central difference time integration scheme. Friction is modeled using a Coulomb law, with a friction coefficient $\mu = 0.15$. Unless otherwise specified, the time step of integration is set to $h = 10^{-7}$ s.

2.3 Contact simulations

A reduced order model of the studied blade is built with the methodology described in section 2.1. As the degrees-of-freedom of 8 nodes are kept in the reduced space, the reduced order model is characterized by a number of boundary degrees-of-freedom $r_b = 24$. For the sake of conciseness, the verification of the methodology is not shown here but is extensively detailed in previous publications [28, 30]. Convergence studies show that it is necessary to include at least $r_c = 15$ internal modes and $r_{\text{MD}} = 150$ modal derivatives in the reduction basis, which leads to a reduction basis of size $r = 189$. The weights associated to each modal derivative and the specific modal derivatives selected

are represented in Fig. 5. The selected modal derivatives ($\star$) correspond to the modal derivatives of the static modes with respect to the generalized coordinates of the static modes (145 MD), the modal derivatives of the first internal mode with respect to the generalized coordinates of the static modes corresponding to the middle of the blade-tip (4 MD) and the modal derivative of the first internal mode with respect to itself (1 MD). More details regarding the selection of the modal derivatives will be given in section 3.1.2. In order to allow the comparison with other studies on NASA rotor 37 blade [47], and contrary to what has been done in [28], the radial direction is here defined as axis $\mathbf{e}_x$ for each boundary node. This explains the minor differences in the interaction maps compared to previous studies.

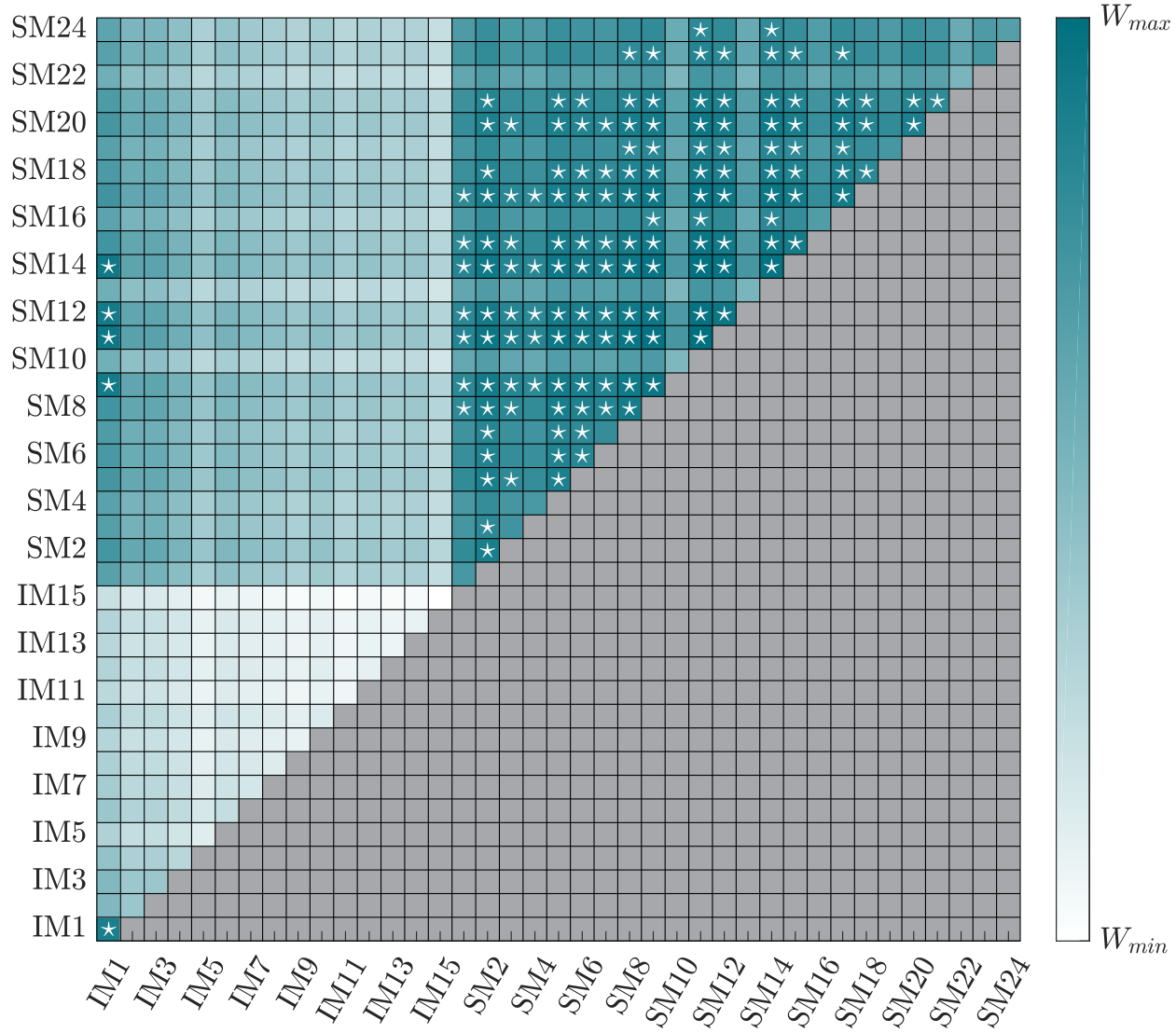

Figure 5. Weights W_{jk} associated to each modal derivative and selected modal derivatives for the contact simulations of the single-blade structure ($\star$).

2.3.1 Interaction maps

The nominal speed of NASA rotor 37 is approximately 1,800 rad/s (17,188.7 RPM in the original report from the NASA [43]). The Campbell diagram plotted in this report allows identifying the main critical speeds. In particular, the intersection with the first bending mode the closest from the nominal speed is linked to the fourth engine order. The methodology is therefore used to study the contact dynamics of the rotating blade on a limited angular speed range around this intersection (denoted by $1B/e_{o4}$). Simulations at constant angular speed Ω between 1,200 rad/s and 1,600 rad/s are performed (with a step of 2 rad/s). For each angular speed, the evolution of the blade tip nodes radial displacement is computed over 200 cycles of revolution, starting from zero initial conditions. The frequency content of the radial displacement is then computed at each angular speed, on the second half of the time signal to get rid of transient effects. The corresponding interaction maps are plotted in Fig. 6a in the case where geometric nonlinearities are not considered and in Fig. 6b in the case where geometric nonlinearities are taken into account. Both maps have the same color scale from blue (lowest amplitudes) to red (highest amplitudes). The first eigenfrequencies and the engine order lines (where the frequency is an integer multiple of the angular speed) are also shown in these maps.

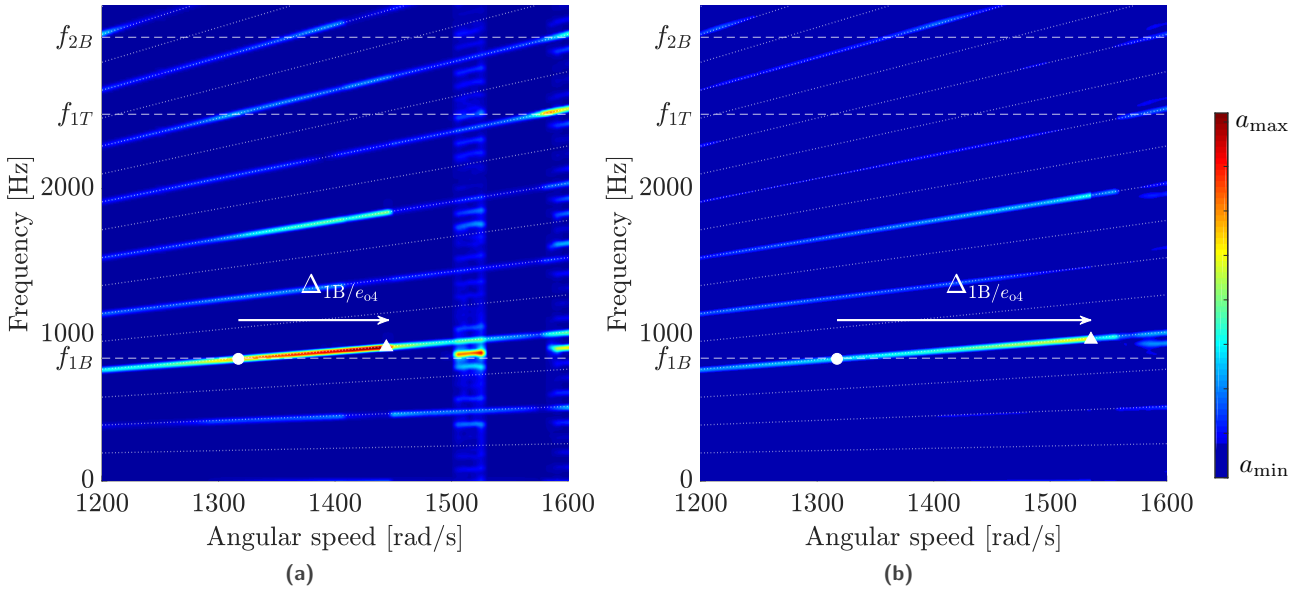

Figure 6. Interaction maps of the radial displacement at node LE with eigenfrequencies (- - -), engine order lines (·····), predicted linear resonance (●) and predicted nonlinear resonance (▲): (a) without geometric nonlinearities and (b) with geometric nonlinearities.

Both interaction maps show lines of higher amplitudes on even engine order lines, which is consistent with the fact that the casing ovalization leads to an excitation occurring twice per revolution. Non-integer harmonics of the angular speed are also visible around 1,525 rad/s in Fig. 6a and around 1,600 rad/s in Fig. 6b, which can be related to the nonlinear nature of the dynamics. It can also be noted that geometric nonlinearities reduce globally the amplitude of vibrations on the whole angular speed range.

The interaction maps highlight the existence of a strong contact interaction between the first bending mode of the blade and the fourth engine order. In both maps, high amplitudes of vibration are followed by amplitude jumps where the amplitude of the displacement suddenly drops for a small change of the angular speed. Because of contact stiffening, the maximal amplitudes are not reached at the exact intersection between the first bending mode line and the fourth engine order line (●) but are shifted toward higher angular speeds (▲). In a linear context, the studied resonance occurs at $\Omega = 1,317$ rad/s. In the case where geometric nonlinearities are neglected, contact stiffening shifts this resonance to $\Omega = 1,446$ rad/s, which corresponds to a contact stiffening of 9.8 %. In the case where

geometric nonlinearities are considered, the contact stiffening seems more pronounced as the maximal amplitudes of vibration occur at $\Omega = 1,535$ rad/s, which corresponds to a contact stiffening of 16.6 %..

In order to better visualize the jump in the amplitude response of the blade in the vicinity of the interaction speed, the infinity norm of the blade's leading edge radial displacement for the same simulations is depicted in Fig. 7 in the cases where geometric nonlinearities are neglected and where they are considered. The curves have been obtained by extracting the maximal radial displacement amplitudes during the last cycle of revolution of each simulation. This figure confirms the previous observations. Geometric nonlinearities seem to be responsible for an additional contact stiffening but give rise to smoother interactions.

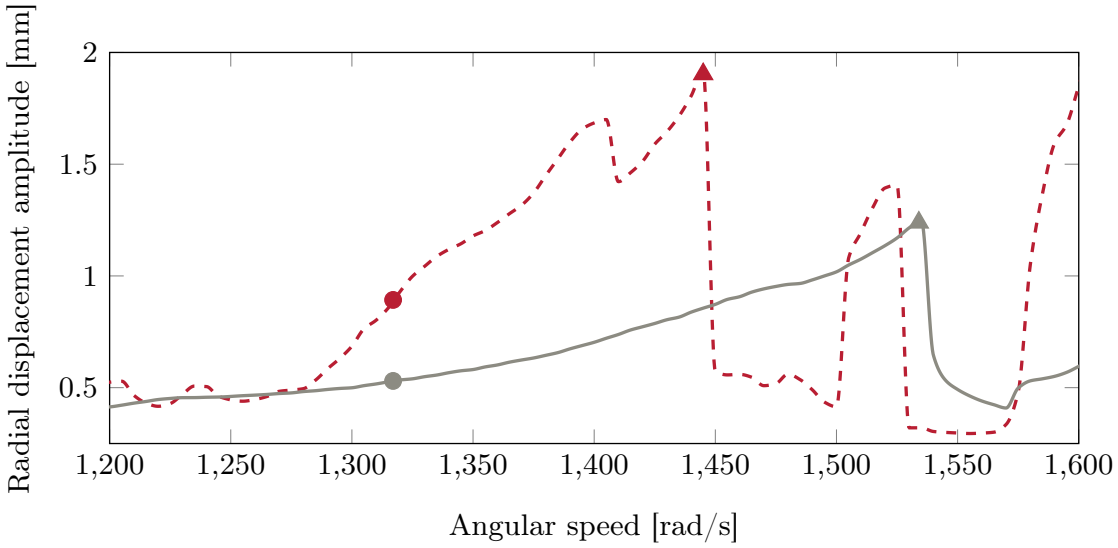

Figure 7. Nonlinear frequency response curve of the radial displacement at node LE in the cases where geometric nonlinearities are not considered (- - -) and where geometric nonlinearities are considered (——) with predicted linear resonance (●) and predicted nonlinear resonance (▲).

More in-depth investigations are performed in the next two sections in order to provide some elements to understand the influence of geometric nonlinearities. First, the clearance consumption of the blade is studied. Clearance consumption has indeed been identified as a key parameter to understand the severity of contact interactions [50]. Then, a continuation procedure is used in the contact simulations.

2.3.2 Clearance consumption

Definition Clearance consumption is a quantity describing the evolution of the clearance between the blade and the casing as the blade vibrates along one of its free vibration modes [50]. The clearance consumption Δ is computed at a given blade-tip node for a given amplitude of deformation δ. It is defined as

$$\Delta(\delta) = c_0 - c(\delta),$$

where c_0 stands for the clearance at rest and $c(\delta)$ stands for the clearance computed at the level of deformation δ. In the following, $\Delta_\delta^{\mathrm{X}}$ and c_δ^{X} respectively denote the clearance consumption and the clearance in deformation mode X at the level of deformation δ. Figure 8 schematically represents the clearance consumption computed for two levels of deformation $\delta = +1$ and $\delta = -1$ for the first bending mode (1B). When $\Delta < 0$, the clearance between the blade and the casing is increased (as for the deformed blade (——) in Fig. 8). When $\Delta > 0$, the clearance between the blade and the casing is decreased (as for the deformed blade (——) in Fig. 8). It should be noted that the clearance is defined as the distance between the blade-tip node considered and its closer counterpart on the casing. Because of the casing conicity (see Fig. 3), the clearance consumption is usually different from the node radial displacement computed in the $\mathrm{O}\mathbf{e}_x\mathbf{e}_y$ plane. These quantities are only equal if the contact surface is perfectly cylindrical.

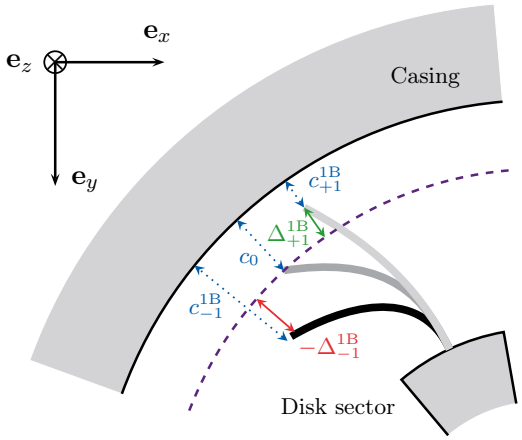

Figure 8. Schematic representation of the clearance consumption with blade at rest (—), bended blade for $\delta = +1$ (—) and bended blade for $\delta = -1$ (—).

Clearance consumption has been identified as a key parameter for the design of blades subjected to contact interactions [51, 50]. Blades with lower clearance consumption, *i.e.* for which the blade/casing clearance remains almost constant as the blade vibrates along its first vibration modes, have been found to feature lower vibration response to contact. Criteria based on the notion of clearance consumption are therefore developed to estimate blade sensitivity to contact interactions and optimize blade profiles [52].

Geometric nonlinearities influence The value of the clearance consumption Δ is looked at over a certain amplitude of deformation such that the radial displacement of the blade-tip node at the leading edge $u_{LE,r}$ satisfies

$$|u_{LE,r}| \leq \zeta, \tag{39}$$

where ζ is a limit value defined further. In practice, a linear modal analysis of the blade finite element model is first performed. This yields the studied mode $\boldsymbol{\phi}^{\mathrm{X}}$, which is normalized so that the radial displacement $u_{LE,r}$ reaches the limit value ζ. A linear static analysis is then performed to recover the external forces $\mathbf{f}_e^{\mathrm{X}}$ that cause the deformation field $\boldsymbol{\phi}^{\mathrm{X}}$. Static analyses with imposed forces $\delta\mathbf{f}_e^{\mathrm{X}}$ are then performed for different values of δ between -1 and $+1$ and the displacement fields (and the corresponding values of the clearance consumption $\Delta_\delta^{\mathrm{X}}$) are computed. These static analyses can be either linear (*i.e.* neglecting the geometric nonlinearities) or nonlinear and therefore allow assessing the influence of geometric nonlinearities. As the procedure is only based on static computations, it can be applied to the full order finite element model and reference results can be obtained.

The clearance consumption is computed as described above at the leading edge (node LE) for the first bending mode and the first torsion mode of the blade. The parameter ζ is fixed to 1 mm for the first bending mode and 0.5 mm for the first torsion mode. The results obtained with the full order finite element model with linear and nonlinear solvers are given in Fig. 9. These results show that the clearance consumption is reduced in both cases when geometric nonlinearities are taken into account. These results justify that the blade with geometric nonlinearities features lower vibration response to contact, as observed in section 2.3.1 when comparing the interactions maps without and with geometric nonlinearities (Fig. 6) and the associated nonlinear frequency response curves (Fig. 7).

The results also highlight that the use of the linear model has to be restricted to small deformations. The relative error made on the clearance consumption with the linear model exceeds 10 % when the level of deformation δ is outside the interval $[-0.25\,,\,0.2]$ for the first bending mode and outside the interval $[-0.1\,,\,0.1]$ for the first torsion mode.

Reduced order model accuracy When studying rubbing phenomena, a very accurate description of the contact interface and of the clearance evolution is required. Reduced order models should therefore be able to evaluate accurately the clearance consumption. As exact results can be computed with the full order finite element model,

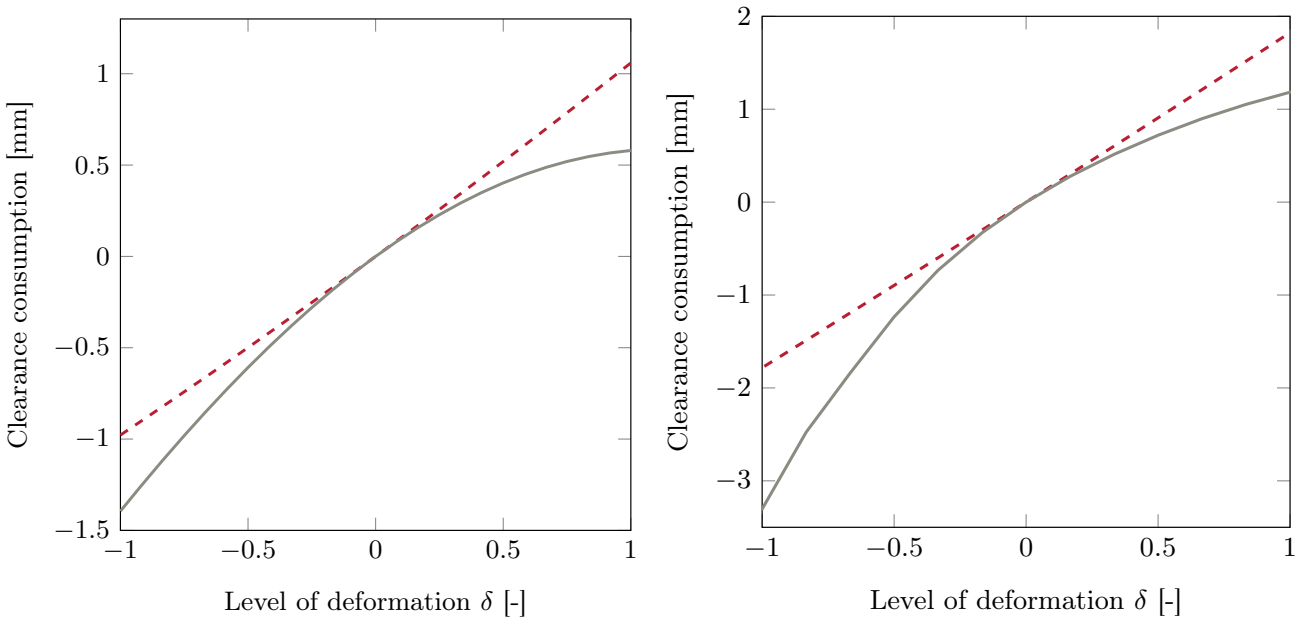

Figure 9. Clearance consumption at the leading edge computed on the full order finite element model with linear (- - -) and nonlinear (——) solvers: (a) first bending mode and (b) first torsion mode.

the accuracy of the ROM can be easily checked by computing the clearance consumption with the ROM itself. The clearance consumption is computed in the same conditions as previously with the reduced order model used in section 2.3.1 characterized by $r_b = 24$, $r_c = 15$ and $r_{\text{MD}} = 150$. In order to show the convergence of the results, the clearance consumption is also computed with two other ROMs: one based on a less rich reduction basis characterized by $r_{\text{MD}} = 100$ and one with a richer reduction basis with $r_{\text{MD}} = 175$. The results accounting for geometric nonlinearities are given in Fig. 10 where they are also compared with the full order model results.

These results confirm that the less rich ROM does not allow for the accurate evaluation of the clearance between the blade and the casing and is therefore not suitable for contact simulations. The results however give confidence in the reduced order model used previously for the contact simulations as it allows computing accurately the clearance consumption (with relative errors less than 10 %). Increasing the number of modal derivatives in the reduction basis does not have a significant influence on the results. As clearance consumption is a key quantity for bladed structures, it is interesting to perform these static analyses before embarking into costly contact simulations. Accurate clearance consumption prediction can be seen as a prerequisite for the reduced order model, even if it does not guarantee the accuracy of the ROM in dynamic simulations.

2.3.3 Nonlinear frequency response curve

The amplitude jumps in Fig. 7 reveal that the numerical procedure does not capture all solutions and that there certainly exist several branches of solutions near these jumps. Such solutions could be obtained by time integration, starting from well chosen initial conditions, or using frequency methods, such as methods derived from the harmonic balance method [47]. With the results in section 2.3.1, there is no way to ensure that the predicted nonlinear resonances are accurate higher amplitude solutions that are not captured with the zero initial conditions used to build the curve could exist.

In order to better quantify the contact stiffening, the nonlinear frequency response curve (NFRC) of the blade is built with the same contact algorithm as in section 2.3.1 combined with a sequential continuation procedure. The continuation procedure consists in performing contact simulations at each angular speed of the studied interval

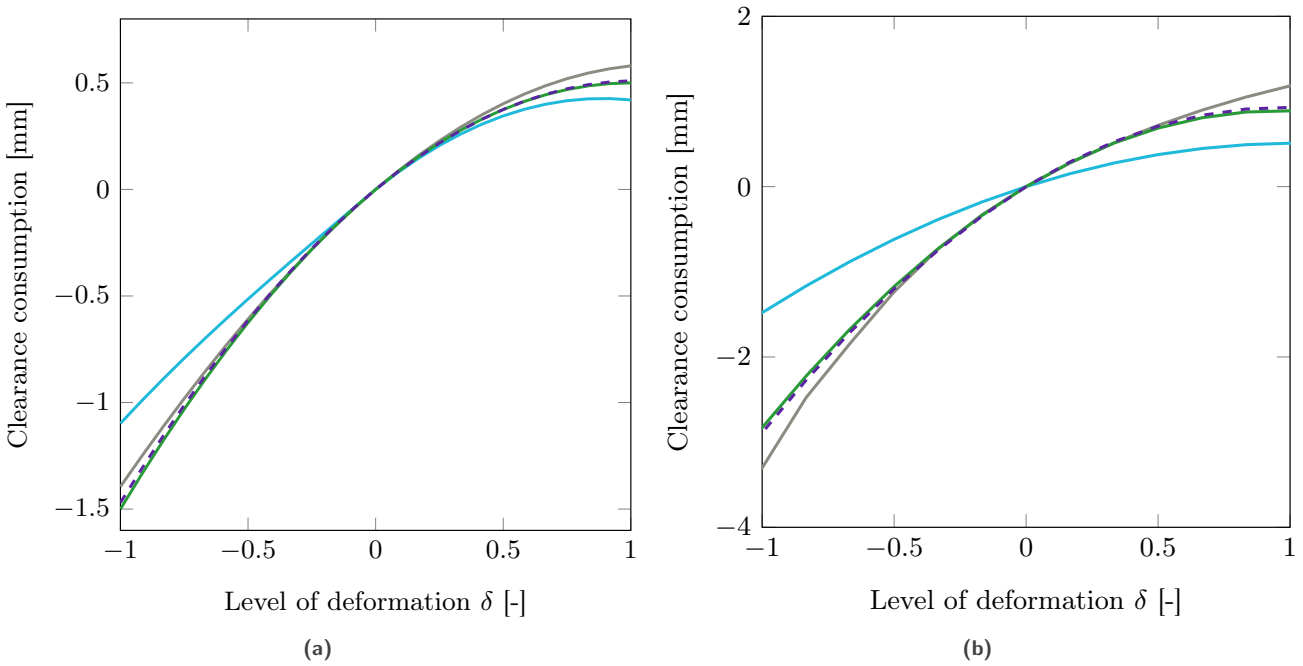

Figure 10. Clearance consumption at the leading edge computed with a nonlinear solver with the full order finite element model (——), the ROMs characterized by $r_b = 24$, $r_c = 15$ and $r_{\text{MD}} = 100$ (——), $r_{\text{MD}} = 150$ (——) and $r_{\text{MD}} = 175$ (- - -): (a) first bending mode and (b) first torsion mode.

successively, taking as initial conditions of simulation i the final conditions of simulation $i-1$. The first contact simulation is conducted over 200 cycles of revolution, in order to reach the steady-state regime, while the following ones are limited to 30 cycles. A step of 2 rad/s is considered. If the steady-state regime is not reached, the step is divided by 2 (with a maximum of 3 divisions). It should be noted that the objective here is not to build the complete nonlinear frequency response curve (with all bifurcations, internal loops, ...), which would require more sophisticated tools, but mainly to correctly assess the contact stiffening. The sequential continuation procedure used here has been validated in the case without geometric nonlinearities by comparison with the results obtained in [47] with a frequency method (RL-HBM). Note that the optimized implementation described in section 2.1.4 cannot be used in this case as it is necessary to wait for the end of simulation i before starting simulation $i+1$.

The nonlinear frequency response curves computed with the continuation procedure (with upward and downward angular speed sweeps) are given in Fig. 11 in the case where geometric nonlinearities are neglected and in Fig. 12 in the case they are considered. These curves are also compared to the curves of Fig. 7 (obtained from zero initial conditions).

These figures confirm that the nonlinear resonances were not correctly captured in Fig. 7 with simulations starting from zero initial conditions as the continuation procedure highlights the existence of higher amplitude solutions. In the case where geometric nonlinearities are neglected, the nonlinear resonance predicted at $\Omega = 1,446$ rad/s (▲) appears to occur at $\Omega = 1,520$ rad/s (■), which corresponds to a contact stiffening of 15.4 %, and leads to amplitudes of vibration more than 50 % greater. In the case where geometric nonlinearities are considered, the nonlinear resonance predicted at $\Omega = 1,535$ rad/s (▲) is only slightly shifted to $\Omega = 1,551$ rad/s (■), which corresponds to a contact stiffening of 17.7 %, and was therefore well approximated in Fig. 7. Neglecting the geometric nonlinearities leads to amplitudes of vibration at the resonance more than two times larger compared to the case with geometric nonlinearities, which is consistent with the clearance consumption analysis in section 2.3.2.

Even if this was not the objective here, the results also show the existence of other branches of solutions that were not captured in Fig. 7 when starting from zero initial conditions. For instance, in the case where geometric

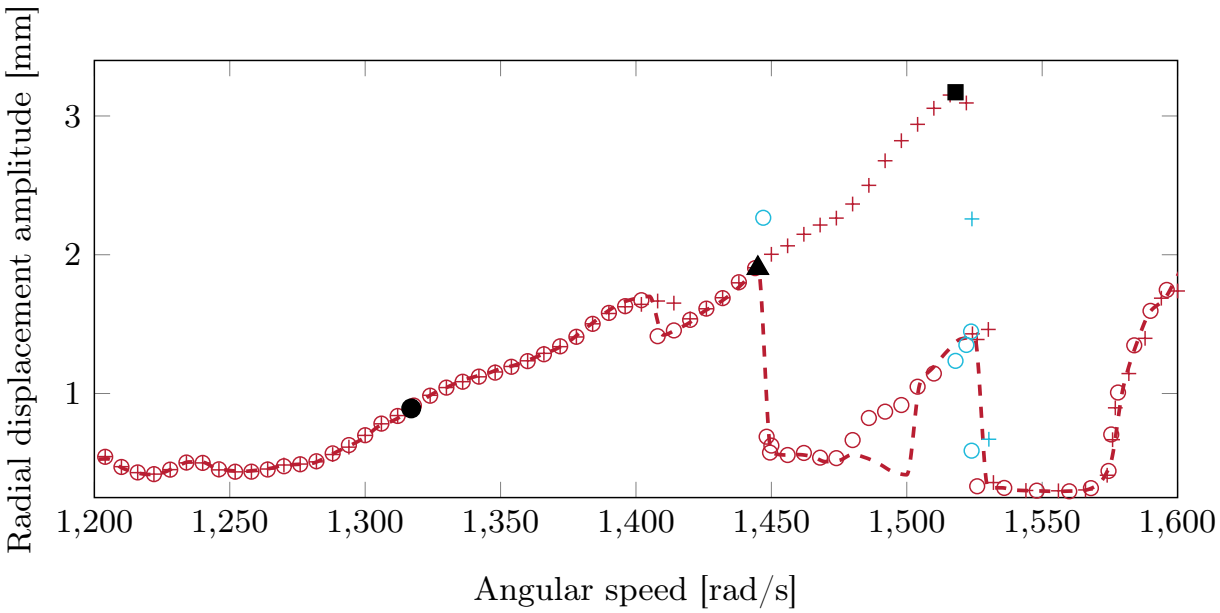

Figure 11. Nonlinear frequency response curve without continuation (- - -) and with continuation (upward (+) and downward (○) angular speed sweeps, simulations where steady-state regime is not reached (+/○)) – without geometric nonlinearities.

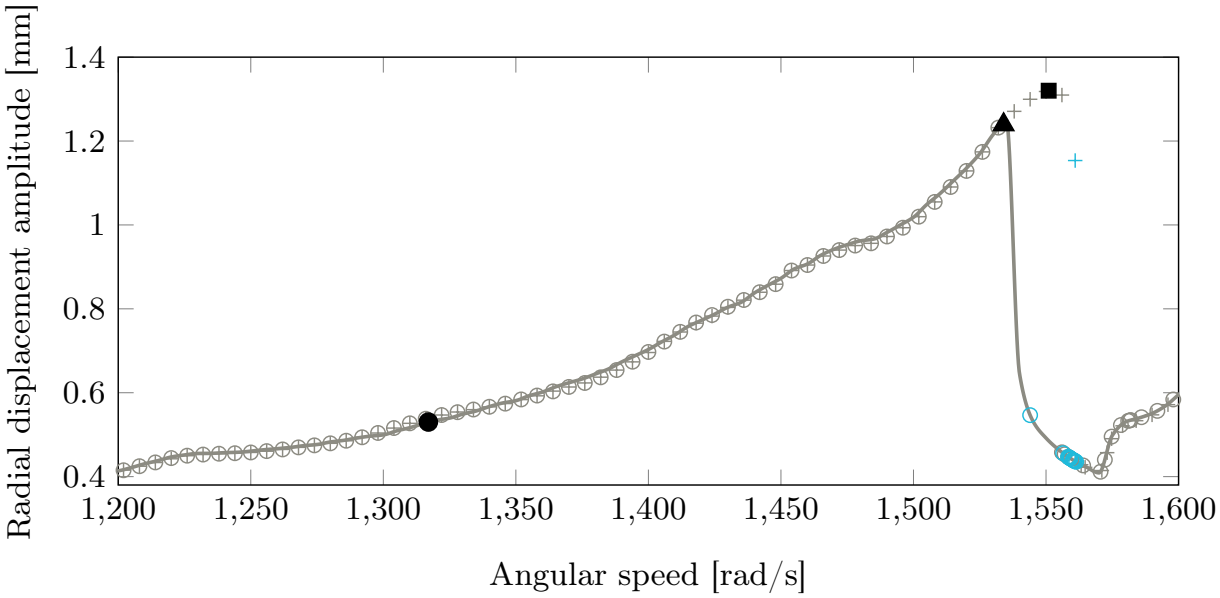

Figure 12. Nonlinear frequency response curve without continuation (- - -) and with continuation (upward (+) and downward (○) angular speed sweeps, simulations where steady-state is not reached (+/○)) – with geometric nonlinearities.

nonlinearities are neglected, Fig. 7 predicts a low-amplitude branch between 1,475 rad/s and 1,500 rad/s with periodic solutions of period $T/2$. Using the continuation procedure with downward angular speed sweep (see Fig. 11), a higher amplitude branch is obtained on the same angular speed interval, with periodic solutions of period $11T/2$.

These results show that the contact stiffening has to be carefully quantified with appropriate tools to follow the

high-amplitude branch of the response and locate correctly the resonance. Also, the observation (in section 2.3.1) that geometric nonlinearities are responsible for a significant additional contact stiffening should be put in perspective. Indeed, results obtained with the continuation procedure show that the contact stiffening with geometric nonlinearities is only slightly greater than the actual stiffening without geometric nonlinearities.

2.4 Partial conclusions

Compared to the first paper dedicated to the development of the methodology and its application to a nonlinear structure [28], the results presented in this paper allow to bring a physical understanding of the nonlinear dynamics of blades and on the influence of geometric nonlinearities. First, the concept of clearance consumption allows to justify why the contact interactions are smoother when geometric nonlinearities are considered. Second, it is shown that the use of a continuation procedure in time-domain allows to better localize the nonlinear resonance and therefore identify the contact stiffening. Contrary to what can be predicted without continuation procedure, the contact stiffening with geometric nonlinearities is, in the studied case, very close to the contact stiffening without geometric nonlinearities.

3 Full bladed disk analysis

In order to study full bladed disks, the single-sector methodology is generalized to multi-sector structures in section 3.1. The bladed disk studied, also based on the NASA rotor 37 blade, is then presented in section 3.2. The methodology is validated in section 3.3 without contact interactions. Lastly, the methodology is used to study the contact interactions of the bladed disk of interest.

3.1 Methodology

The single-sector methodology recalled in section 2.1 is combined to a Component Mode Synthesis (CMS) technique and extended to multi-sector structures. The bladed structure is divided into N identical sectors composed of one blade and the corresponding disk sector (see Fig. 13). The degrees-of-freedom of sector n ($n = 1, \dots, N$), $\mathbf{u}^n$, are partitioned according to

$$\mathbf{u}^n = \begin{bmatrix} \mathbf{u}^n_{\text{left}} \\ \mathbf{u}^n_i \\ \mathbf{u}^n_b \\ \mathbf{u}^n_{\text{right}} \end{bmatrix}, \tag{40}$$

where $\mathbf{u}^n_{\text{left}}$ and $\mathbf{u}^n_{\text{right}}$ respectively stand for the n_{left} and n_{right} degrees-of-freedom of the left and right cyclic boundaries (with $n_{\text{left}} = n_{\text{right}}$ because of mesh compatibility), $\mathbf{u}^n_b$ stands for the r_b boundary degrees-of-freedom that are kept in the reduced space (*i.e.* the blade-tip degrees-of-freedom) and $\mathbf{u}^n_i$ stands for the n_i internal degrees-of-freedom that do not belong to any boundary. The sectors are mechanically coupled through the cyclic boundary degrees-of-freedom.

3.1.1 Reduction basis

In the proposed methodology, each sector is reduced following the methodology presented in section 2.1, *i.e.* projected onto a basis composed of Craig-Bampton modes and a selection of their modal derivatives. The boundary degrees-of-freedom of the single-sector methodology are here defined as the blade-tip degrees-of-freedom and the cyclic boundaries. The reduction of the degrees-of-freedom of sector n therefore writes

$$\mathbf{u}^n = \begin{bmatrix} \mathbf{u}^n_{\text{left}} \\ \mathbf{u}^n_i \\ \mathbf{u}^n_b \\ \mathbf{u}^n_{\text{right}} \end{bmatrix} = \begin{bmatrix} \mathbf{I} & \mathbf{0} & \mathbf{0} & \mathbf{0} \\ \boldsymbol{\Psi}^n_{\text{left}} & \boldsymbol{\Phi}^n & \boldsymbol{\Psi}^n_b & \boldsymbol{\Psi}^n_{\text{right}} \\ \mathbf{0} & \mathbf{0} & \mathbf{I} & \mathbf{0} \\ \mathbf{0} & \mathbf{0} & \mathbf{0} & \mathbf{I} \end{bmatrix} \begin{bmatrix} \mathbf{u}^n_{\text{left}} \\ \boldsymbol{\eta}^n \\ \mathbf{u}^n_b \\ \mathbf{u}^n_{\text{right}} \end{bmatrix}; \tag{41}$$

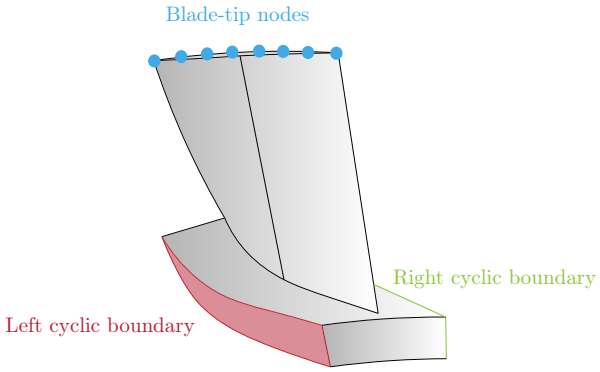

Figure 13. Bladed disk sector with simplified representation of the disk.

where $\boldsymbol{\Psi}^n_{\text{left}}$, $\boldsymbol{\Psi}^n_{\text{right}}$ and $\boldsymbol{\Psi}^n_b$ are the constraint modes corresponding to the static deformations of the sector to unit displacements imposed respectively at the degrees-of-freedom $\mathbf{u}^n_{\text{left}}$, $\mathbf{u}^n_{\text{right}}$ and $\mathbf{u}^n_b$ (computed as in Eq. (9)) and

$$\boldsymbol{\Phi}^n = \begin{bmatrix} \boldsymbol{\Theta}^n_{i,r_c} & \mathbf{Z}^n \end{bmatrix}, \tag{42}$$

where $\boldsymbol{\Theta}^n_{i,r_c}$ are the first r_c linear normal modes of the sector clamped at the boundary degrees-of-freedom (computed as in Eq. (11)) and $\mathbf{Z}^n$ are r_{MD} modal derivatives of the sector (computed as in Eq. (17)). The modal derivatives have to be carefully selected according to a selection criterion. Different selection criteria are presented in section 3.1.2. In the case of a tuned structure, the matrices $\boldsymbol{\Psi}^n_{\text{left}}$, $\boldsymbol{\Phi}^n$, $\boldsymbol{\Psi}^n_b$ and $\boldsymbol{\Psi}^n_{\text{right}}$ are respectively identical for each value of n between 1 and N and the reduction basis is only computed once. The methodology is however not restricted to tuned structures. Considering the cyclic conditions

$$\mathbf{u}^n_{\text{left}} = \mathbf{u}^{n-1}_{\text{right}} \quad (n = 2, \dots, N) \quad \text{and} \quad \mathbf{u}^1_{\text{left}} = \mathbf{u}^N_{\text{right}} \tag{43}$$

and regrouping the cyclic boundary degrees-of-freedom in

$$\mathbf{u}_{\text{cyclic}} = \begin{bmatrix} \mathbf{u}^1_{\text{left}} \\ \vdots \\ \mathbf{u}^N_{\text{left}} \end{bmatrix}, \tag{44}$$

the reduction of the multi-sector structure writes

$$\mathbf{u} = \begin{bmatrix} \mathbf{u}^1_i \\ \mathbf{u}^1_b \\ \vdots \\ \mathbf{u}^N_i \\ \mathbf{u}^N_b \\ \mathbf{u}_{\text{cyclic}} \end{bmatrix} = \begin{bmatrix} \boldsymbol{\Phi}^1 & \boldsymbol{\Psi}^1_b & \cdots & \mathbf{0} & \mathbf{0} & \boldsymbol{\Psi}^1_{\text{cyclic}} \\ \mathbf{0} & \mathbf{I} & \cdots & \mathbf{0} & \mathbf{0} & \mathbf{0} \\ \vdots & \vdots & \ddots & \vdots & \vdots & \vdots \\ \mathbf{0} & \mathbf{0} & \cdots & \boldsymbol{\Phi}^N & \boldsymbol{\Psi}^N_b & \boldsymbol{\Psi}^N_{\text{cyclic}} \\ \mathbf{0} & \mathbf{0} & \cdots & \mathbf{0} & \mathbf{I} & \mathbf{0} \\ \mathbf{0} & \mathbf{0} & \cdots & \mathbf{0} & \mathbf{0} & \mathbf{I} \end{bmatrix} \begin{bmatrix} \boldsymbol{\eta}^1 \\ \mathbf{u}^1_b \\ \vdots \\ \boldsymbol{\eta}^N \\ \mathbf{u}^N_b \\ \mathbf{u}_{\text{cyclic}} \end{bmatrix}, \tag{45}$$

where

$$\begin{aligned} \boldsymbol{\Psi}^n_{\text{cyclic}} &= \begin{bmatrix} \mathbf{0}_{n_i \times (n-1) n_{\text{left}}} & \boldsymbol{\Psi}^n_{\text{left}} & \boldsymbol{\Psi}^n_{\text{right}} & \mathbf{0}_{n_i \times (N-n-1) n_{\text{left}}} \end{bmatrix} \quad (n = 1, \dots, N-1) \\ \text{and} \quad \boldsymbol{\Psi}^N_{\text{cyclic}} &= \begin{bmatrix} \boldsymbol{\Psi}^N_{\text{right}} & \mathbf{0}_{n_i \times (N-2) n_{\text{left}}} & \boldsymbol{\Psi}^N_{\text{left}} \end{bmatrix}. \end{aligned} \tag{46}$$

In a more compact form, defining

$$\bar{\mathbf{u}}^n = \begin{bmatrix} \mathbf{u}_i^n \\ \mathbf{u}_b^n \end{bmatrix}, \tag{47}$$

the reduction writes

$$\mathbf{u} = \begin{bmatrix} \bar{\mathbf{u}}^1 \\ \vdots \\ \bar{\mathbf{u}}^N \\ \mathbf{u}_{\text{cyclic}} \end{bmatrix} = \begin{bmatrix} \bar{\mathbf{\Phi}}^1 & \cdots & \mathbf{0} & \bar{\mathbf{\Psi}}^1_{\text{cyclic}} \\ \vdots & \vdots & \ddots & \vdots \\ \mathbf{0} & \cdots & \bar{\mathbf{\Phi}}^N & \bar{\mathbf{\Psi}}^N_{\text{cyclic}} \\ \mathbf{0} & \cdots & \mathbf{0} & \mathbf{I} \end{bmatrix} \begin{bmatrix} \mathbf{q}^1 \\ \vdots \\ \mathbf{q}^N \\ \mathbf{u}_{\text{cyclic}} \end{bmatrix} = \mathbf{\Phi}_{\text{I}} \hat{\mathbf{q}}, \tag{48}$$

where

$$\bar{\mathbf{\Phi}}^n = \begin{bmatrix} \mathbf{\Phi}^n & \mathbf{\Psi}_b^n \\ \mathbf{0} & \mathbf{I} \end{bmatrix} \quad \text{and} \quad \bar{\mathbf{\Psi}}^n_{\text{cyclic}} = \begin{bmatrix} \mathbf{\Psi}^n_{\text{cyclic}} \\ \mathbf{0} \end{bmatrix}. \tag{49}$$

This first projection onto the reduced basis $\mathbf{\Phi}_{\text{I}}$ leads to a reduced order model of size $N(r_c + r_{\text{MD}} + r_b + n_{\text{left}})$. For industrial finite element models, n_{left} may be very large and a second reduction of the system is then required. Many works regarding interface reduction in substructuring methods can be found in the literature [53]. Here, a modal reduction of the cyclic boundary degrees-of-freedom is performed. Denoting by $\hat{\mathbf{K}}$ and $\hat{\mathbf{M}}$ the projections of the stiffness and mass matrices onto $\mathbf{\Phi}_{\text{I}}$, the modes $\mathbf{\Pi}$ related to the sub-matrices corresponding to the cyclic boundary degrees-of-freedom are computed as

$$\hat{\mathbf{K}}_{\text{cyclic}} \mathbf{\Pi} = \hat{\mathbf{M}}_{\text{cyclic}} \mathbf{\Pi} \boldsymbol{\omega}^2. \tag{50}$$

The second reduction writes

$$\hat{\mathbf{q}} = \begin{bmatrix} \mathbf{q}^1 \\ \vdots \\ \mathbf{q}^N \\ \mathbf{u}_{\text{cyclic}} \end{bmatrix} = \begin{bmatrix} \mathbf{I} & \cdots & \mathbf{0} & \mathbf{0} \\ \vdots & \ddots & \mathbf{0} & \mathbf{0} \\ \mathbf{0} & \cdots & \mathbf{I} & \mathbf{0} \\ \mathbf{0} & \cdots & \mathbf{0} & \mathbf{\Pi}_{r_{\text{cyclic}}} \end{bmatrix} \begin{bmatrix} \mathbf{q}^1 \\ \vdots \\ \mathbf{q}^N \\ \boldsymbol{\eta}_{\text{cyclic}} \end{bmatrix} = \mathbf{\Phi}_{\text{II}} \mathbf{q}, \tag{51}$$

where $\mathbf{\Pi}_{r_{\text{cyclic}}}$ is formed by extracting from $\mathbf{\Pi}$ the r_{cyclic} modes whose frequencies are the closest from the frequencies of modes $\mathbf{\Theta}^n_{i,r_c}$ $(n = 1, \ldots, N)$. Combining Eq. (48) and Eq. (51), the complete reduction writes

$$\mathbf{u} = \mathbf{\Phi}_{\text{I}} \mathbf{\Phi}_{\text{II}} \mathbf{q} = \mathbf{\Phi} \mathbf{q}. \tag{52}$$

The size of the reduced order model is therefore given by

$$r = N(r_c + r_{\text{MD}} + r_b) + r_{\text{cyclic}}. \tag{53}$$

3.1.2 Modal derivatives selection criterion

The size of the reduction basis increases quadratically with the number of Craig-Bampton modes. However, it is expected that only a few modal derivatives are necessary to capture the nonlinear behavior of the structure [54]. In order to limit the size of the reduction basis, it is necessary to define a selection criterion that allows to determine *a priori* which modal derivatives have to be included in the reduction basis to achieve accurate results. Different selection procedures exist in the literature but they are often limited to the selection of modal derivatives of linear normal modes, and not of Craig-Bampton modes as in this work [54, 55, 56]. As orthogonality properties of linear normal modes do not hold for Craig-Bampton modes, these selection criteria have to be adapted. Three selection criteria are presented here. They all consist in associating a weight W^n_{jk} to each modal derivative $\boldsymbol{\zeta}^n_{jk}$ of sector n and selecting the best modal derivative subset based on the magnitude of these weights, the highest values of the weight corresponding to the most relevant modal derivatives. The selection methods are purely heuristic methods that differ by the definition of the weight. These criteria are applied to the studied test case and compared in section 3.3.1.

Maximum Modal Interaction (MMI) The first way of computing the weights is adapted from [54]. The linear response $\mathbf{u}(t)$ of the system to a given external loading is computed with the full order finite element model by solving Eq. (1) where the nonlinear terms are neglected ($\mathbf{g}_{\text{nl}}(\mathbf{u}) = \mathbf{0}$ and $\mathbf{f}_c(\mathbf{u}, \dot{\mathbf{u}}) = \mathbf{0}$). The response is expressed in the Craig-Bampton reduced space through Eq. (2), where $\mathbf{\Phi}$ is the linear Craig-Bampton basis. Assuming that the contribution of the modal derivatives is of second order, their mutual relevance could be indicated by

$$W_{jk}^{(1)} = |\boldsymbol{\phi}_j| \max(|q_j(t)|) \cdot |\boldsymbol{\phi}_k| \max(|q_k(t)|). \tag{54}$$

The actual interaction between the modes is not investigated. It is only assumed that two Craig-Bampton modes that bear a relevant part of the reduced solution are likely to interact.

Modal Interaction (MI) Going one step further, it is proposed in [55] to consider the complete interaction between the linear modes in the simulation of duration T. The weights are defined as

$$W_{jk}^{(2\text{a})} = \int_0^T |q_j(t) q_k(t)| dt, \tag{55}$$

with mass-normalized modes. Alternatively, the weights can also be defined as

$$W_{jk}^{(2\text{b})} = |\boldsymbol{\phi}_j^{\text{T}} \boldsymbol{\phi}_k| \int_0^T |q_j(t) q_k(t)| dt, \tag{56}$$

with no assumption over the modes normalization.

Symmetric Modal Virtual Work (SMVW) In this criterion, weights are assigned to modal derivatives according to the virtual work done by the nonlinear elastic forces arising from one linear mode upon another mode. This criterion is introduced in [55] and adapted in [56] for static modal derivatives, *i.e.* obtained by neglecting the inertial contribution, as it is done here. The criterion is used here in the case of Craig-Bampton modes. As above, linear simulations allow computing the time varying amplitude of each linear generalized coordinate. For each pair of modes, the time $t_{ij}^{\max}$ is determined by

$$t_{ij}^{\max} = \arg\max \left[q_i(t) q_j(t)\right]^2. \tag{57}$$

The virtual work of mode pair $\boldsymbol{\phi}_j$ and $\boldsymbol{\phi}_k$ is defined in a symmetric way as

$$W_{jk}^{(3)} = \sqrt{\left[\boldsymbol{\phi}_k^{\text{T}} \mathbf{g}_{\text{nl}}\left(\boldsymbol{\phi}_j q_j(t_{ij}^{\max})\right)\right]^2 + \left[\boldsymbol{\phi}_j^{\text{T}} \mathbf{g}_{\text{nl}}\left(\boldsymbol{\phi}_k q_k(t_{ij}^{\max})\right)\right]^2}. \tag{58}$$

3.1.3 Reduced nonlinear internal forces

The nonlinear internal forces write

$$\mathbf{g}_{\text{nl}}(\mathbf{u}) = \begin{bmatrix} \bar{\mathbf{g}}_{\text{nl}}^1(\mathbf{u}) \\ \vdots \\ \bar{\mathbf{g}}_{\text{nl}}^N(\mathbf{u}) \\ \mathbf{g}_{\text{nl}}^{\text{cyclic}}(\mathbf{u}) \end{bmatrix}, \tag{59}$$

where $\bar{\mathbf{g}}_{\text{nl}}^n(\mathbf{u})$ stands for the forces on degrees-of-freedom $\bar{\mathbf{u}}^n$ and $\mathbf{g}_{\text{nl}}^{\text{cyclic}}(\mathbf{u})$ for the forces on degrees-of-freedom $\mathbf{u}_{\text{cyclic}}$. Their projection on the reduced basis $\mathbf{\Phi}$ is computed as in Eq. (5) and writes

$$\tilde{\mathbf{g}}_{\text{nl}}(\mathbf{q}) = \begin{bmatrix} \tilde{\mathbf{g}}_{\text{nl}}^1(\mathbf{q}) \\ \vdots \\ \tilde{\mathbf{g}}_{\text{nl}}^N(\mathbf{q}) \\ \tilde{\mathbf{g}}_{\text{nl}}^{\text{cyclic}}(\mathbf{q}) \end{bmatrix} = \begin{bmatrix} \bar{\mathbf{\Phi}}^{1^{\text{T}}} \bar{\mathbf{g}}_{\text{nl}}^1(\mathbf{\Phi q}) \\ \vdots \\ \bar{\mathbf{\Phi}}^{N^{\text{T}}} \bar{\mathbf{g}}_{\text{nl}}^N(\mathbf{\Phi q}) \\ \mathbf{\Pi}_{r_{\text{cyclic}}}^{\text{T}} \left[\sum_{k=1}^N \bar{\mathbf{\Psi}}_{\text{cyclic}}^{k^{\text{T}}} \bar{\mathbf{g}}_{\text{nl}}^k(\mathbf{\Phi q}) + \mathbf{g}_{\text{nl}}^{\text{cyclic}}(\mathbf{\Phi q})\right] \end{bmatrix} \tag{60}$$

In order to extend the CMS procedure to the computation of these nonlinear forces, it is assumed that the constraint modes related to the cyclic boundaries remain linear. This assumption, also made in [57] and [20], implies the linearity of the couplings between the substructures. In the case of bladed structures, the sectors are connected by a relatively thick and stiff disk. Geometric nonlinear effects can occur in the blade, but it seems justified to assume that the displacement of the disk remains small and, therefore, that the degrees-of-freedom of the disk boundaries are linear. In this context, the internal forces in each sector are also simplified. It is assumed that the reduced nonlinear internal forces in sector n ($n = 1, \dots, N$), $\tilde{\mathbf{g}}_{\text{nl}}^n$, only depend on the internal and blade-tip generalized coordinates of the sector, $\mathbf{q}^n$. The projected nonlinear internal forces therefore write

$$\tilde{\mathbf{g}}_{\text{nl}}(\mathbf{q}) = \begin{bmatrix} \tilde{\mathbf{g}}_{\text{nl}}^1(\mathbf{q}^1) \\ \vdots \\ \tilde{\mathbf{g}}_{\text{nl}}^N(\mathbf{q}^N) \\ \mathbf{0} \end{bmatrix} = \begin{bmatrix} \bar{\mathbf{\Phi}}^{1^{\mathrm{T}}} \bar{\mathbf{g}}_{\text{nl}}^1(\bar{\mathbf{\Phi}}^1 \mathbf{q}^1) \\ \vdots \\ \bar{\mathbf{\Phi}}^{N^{\mathrm{T}}} \bar{\mathbf{g}}_{\text{nl}}^N(\bar{\mathbf{\Phi}}^N \mathbf{q}^N) \\ \mathbf{0} \end{bmatrix}. \tag{61}$$

Under these assumptions, the STEP presented in section 2.1.2 can be applied to compute the reduced nonlinear internal forces of each sector. The nonlinear internal forces of sector n are expressed as the polynomial

$$\tilde{\mathbf{g}}_{\text{nl}}^n(\mathbf{q}^n) = \tilde{\boldsymbol{\mathcal{A}}}^n(\mathbf{q}^n, \mathbf{q}^n) + \tilde{\boldsymbol{\mathcal{B}}}^n(\mathbf{q}^n, \mathbf{q}^n, \mathbf{q}^n), \tag{62}$$

using a functional notation for the quadratic and cubic terms with coefficients gathered in the third-order tensor $\tilde{\mathbf{A}}^n$ and the fourth-order tensor $\tilde{\mathbf{B}}^n$. Components of the tensors $\tilde{\mathbf{A}}^n$ and $\tilde{\mathbf{B}}^n$ are determined as described in section 2.1.2. The nonlinear forces static evaluations are performed on the sector finite element model clamped at the cyclic boundaries degrees-of-freedom and with imposed displacements defined as linear combinations of the modes $\bar{\mathbf{\Phi}}^n$. In the case of tuned structures, the tensors $\tilde{\mathbf{A}}^n$ (and respectively $\tilde{\mathbf{B}}^n$) are identical for each sector n and have to be computed only once. In the case of detuned structures, one STEP analysis has to be performed for each kind of sector. These analyses are independent and can be performed in parallel.

3.1.4 Contact treatment

The strategy described in section 2.1.3 for single-sector structures is also valid for multi-sector structures and does not need to be adapted. At each time step, possible penetrations are computed at the boundary degrees-of-freedom $\mathbf{u}_b^n$ ($n = 1, \dots, N$) corresponding to the blade-tip nodes of the N sectors.

3.2 Test case

The methodology is applied on an industrial bladed-disk model based on the NASA rotor 37 blade. A disk sector is added to the blade model presented in section 2.2.1, as shown in Fig. 14. Note that the height of the blade is decreased by 4 mm compared to section 2.2.1 in order to ensure a good merge between the blade and the disk. The 36 sectors of the bladed disk are assumed to be identical. The discretized mesh counts 44,535 nodes per sector, *i.e.* 133,605 degrees-of-freedom. The sectors are clamped at the disk lower surfaces. Material properties are identical to the ones given in section 2.2.1.

Based on this finite element model, the SAFE diagram (Singh's Advanced Frequency Evaluation diagram, *i.e.* the eigenfrequencies as a function of the number of nodal diameters), is computed and represented in Fig. 15. Different mode families exist: modes dominated by blade deformation (corresponding to the successive bending and torsion modes of the blade) and modes with high participation of the disk.

3.3 Verification without contact

In order to validate the proposed methodology, the reduction procedure is first applied on the bladed disk of interest subjected to an equivalent aerodynamic loading of sufficiently high amplitude to activate geometric nonlinear effects. Contact interactions are not considered in this section. The scalar performance indicator I introduced in [28] is used to assess the accuracy of the reduction method. This performance indicator is defined as a weighted sum of four different criteria that allow quantifying the accuracy of the reduced order model both locally (at the blade tips) and globally. It ranges from 0 to 1, the closer to one, the better the reduction method.

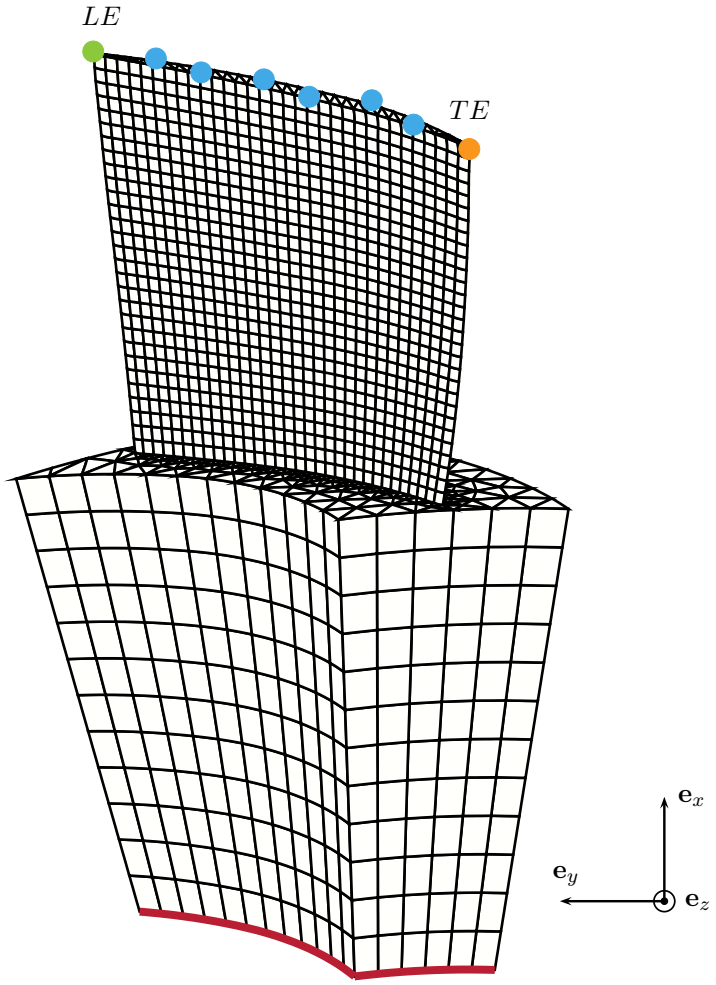

Figure 14. Single sector of NASA rotor 37 with mesh used for the finite element simulations and clamped surface (■). The eight colored nodes are the blade tip nodes used further for the definition of the excitation and for contact simulations. Among those nodes, the node TE is located at the trailing edge (●) and the node LE is located at the leading edge (●).

3.3.1 Comparison of modal derivatives selection criterion

In this section, the performance indicator introduced in [28] is used to evaluate and compare the different modal derivatives selection criteria defined in section 3.1.2. Different reduced order models are built with $r_b = 3$ degrees-of-freedom per sector (corresponding to the nodes LE of each sector, see Fig. 14) kept in the reduced space. The reduction bases are composed of $r_c = 10$ internal modes per sector and $r_{\text{MD}} = 10$ modal derivatives per sector selected according to the different criteria of section 2.1.1. The training excitation, used in the dynamic simulation required for the weights computation, is defined as a harmonic excitation of amplitude $A_t = 400$ N and pulsation $\omega_t = 4,000$ rad/s applied at $N_t = 1$ node (node LE) in the $\mathbf{e}_z$ direction. This excitation mainly excites the first blade mode family (see SAFE diagram in Fig. 15). The second reduction is characterized by $r_{\text{cyclic}} = 144$. This leads to reduced order models of size $r = 972$.

The reduced order models are used to compute the response of the structure to a harmonic excitation of amplitude $A_e = A_t$ and pulsation $\omega_e = \omega_t$ (period T) applied at $N_e = 1$ node per sector (nodes LE) in the $\mathbf{e}_z$ direction (0-diameter excitation – $N_d = 0$). The transient and steady-state responses at the excited blade tip node obtained

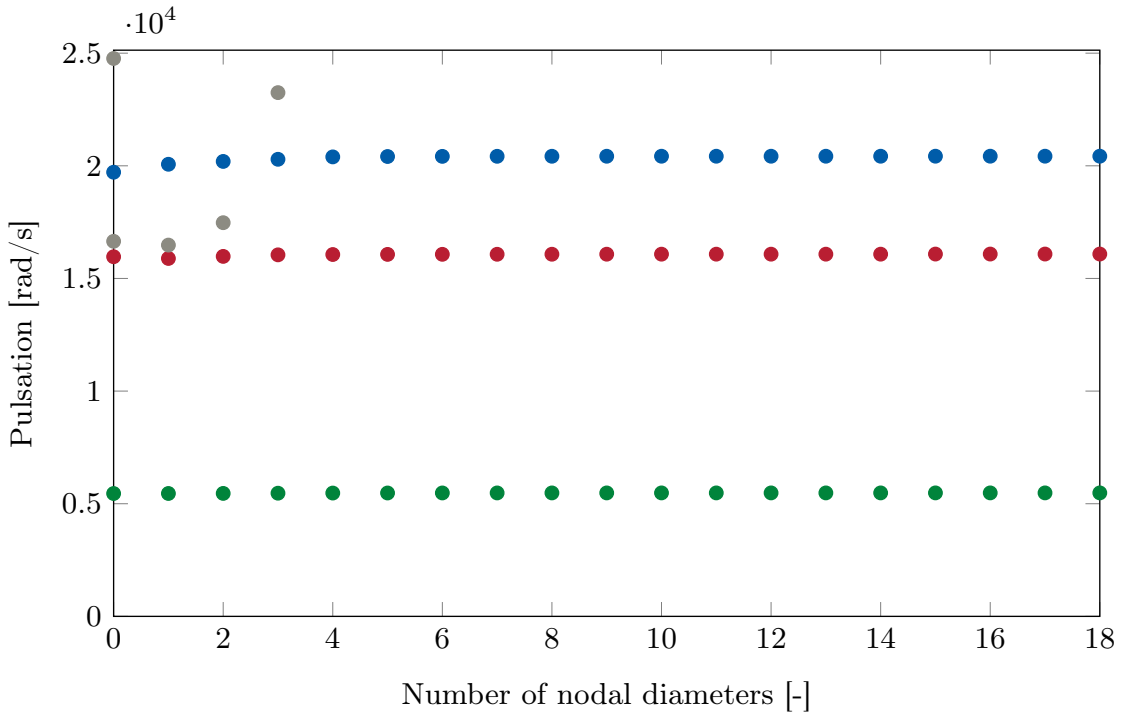

Figure 15. SAFE diagram of the studied bladed disk for mode families 1B (●), 1T (●) and 2B (●) and disk-dominated modes (●).

with the full order model are shown in Fig. 16 in the cases where geometric nonlinearities are considered and when they are not. The results in these figures highlight that the amplitude of the excitation is sufficient to activate the geometric nonlinear effects as significant differences in the responses are evidenced.

The absolute errors between the responses computed with the reduced order models and the reference nonlinear solution computed with the full order model are shown in Fig. 17a and Fig. 17b. The error obtained with a reduction basis composed of $r_{\mathrm{MD}} = 10$ randomly chosen modal derivatives is also represented in Fig. 17a.

Qualitatively, the results underline the importance of defining a good selection criterion for the modal derivatives. Whereas small errors are observed for the selection criteria 1 to 3, the solution obtained with the randomly chosen modal derivatives is very inaccurate, even worse than simply neglecting the geometric nonlinearities. These results also allow to quantitatively assess the relevance of each selection criterion. Among the studied criteria, criteria 2a and 2b yield the best results, followed by criterion 1 and criterion 3. All the criteria allow capturing the nonlinear features of the response. Quantitatively, the performance indicator is given by $I = 0.93$ for criterion 1, $I = 0.96$ for criterion 2a, $I = 0.97$ for criterion 2b, and $I = 0.91$ for criterion 3. Other studies, which are not detailed here for the sake of conciseness, have been performed with other external excitations and confirm the choice of the selection criterion 2b for the next analyses.

The transient response obtained with criterion 2b is then compared with the response computed with a reduction basis where all $r_{\mathrm{MD}} = 91$ modal derivatives are included. The corresponding absolute error is shown in Fig. 18a. The addition of the remaining 81 modal derivatives in the reduction basis does not significantly enhance the performance of the reduction method. Indeed, the performance indicator is only slightly increased to $I = 0.98$ while the size r of the reduction basis is multiplied by a factor 4. These results confirm that it is not necessary to include all modal derivatives in the reduction basis to have good performance. This selection criterion is therefore a powerful tool that allows the reduction of the size of the reduction basis while ensuring an accurate prediction of the structure dynamic response.

The absolute errors on the steady-state responses computed with the different reduction bases are shown in

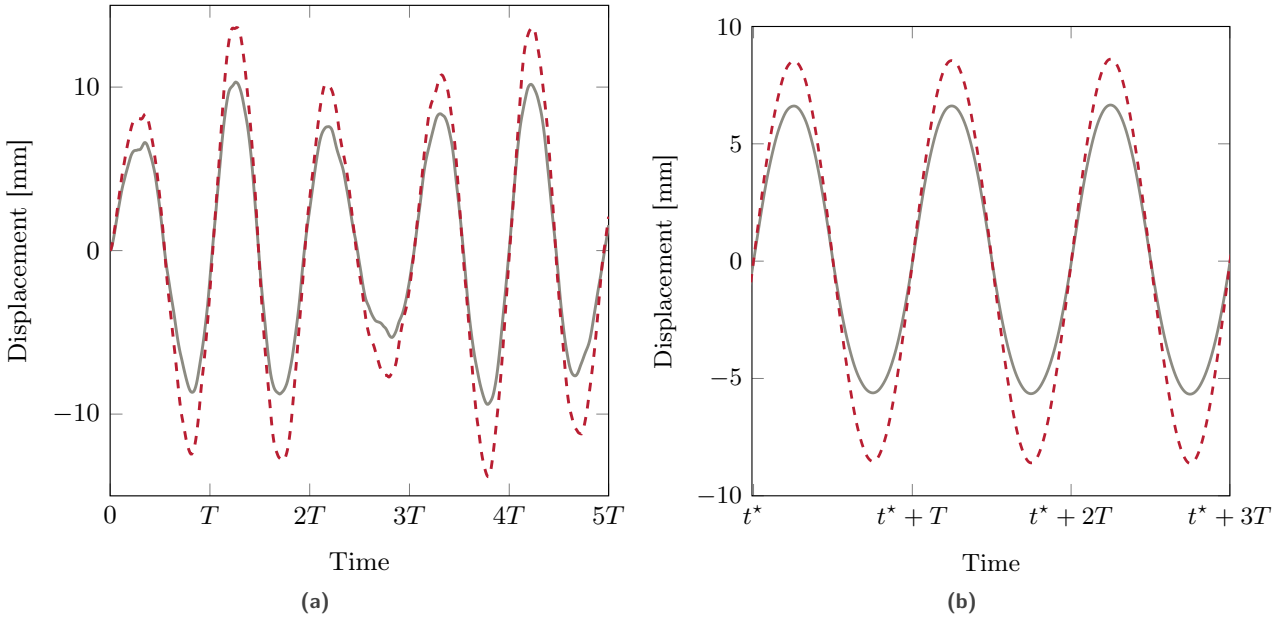

Figure 16. Linear (- - -) and nonlinear (——) responses of the blade at node LE in the $\mathbf{e}_z$ direction computed with the full order finite element model: (a) transient response and (b) steady-state response.

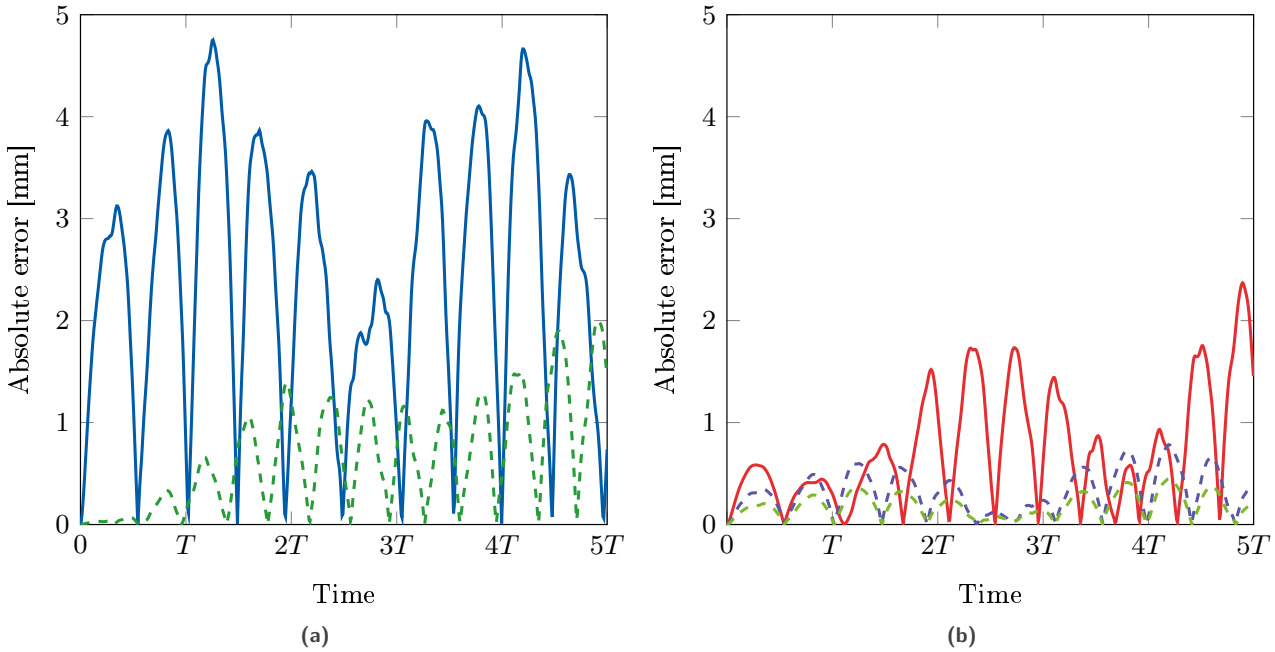

Figure 17. Absolute errors between the nonlinear responses predicted with the full order model and the reduced order models with: (a) 10 randomly chosen modal derivatives (——), the 10 modal derivatives selected with criterion 1 (- - -) and (b) the 10 modal derivatives selected with criterion 2a (- - -), criterion 2b (- - -) and criterion 3 (——).

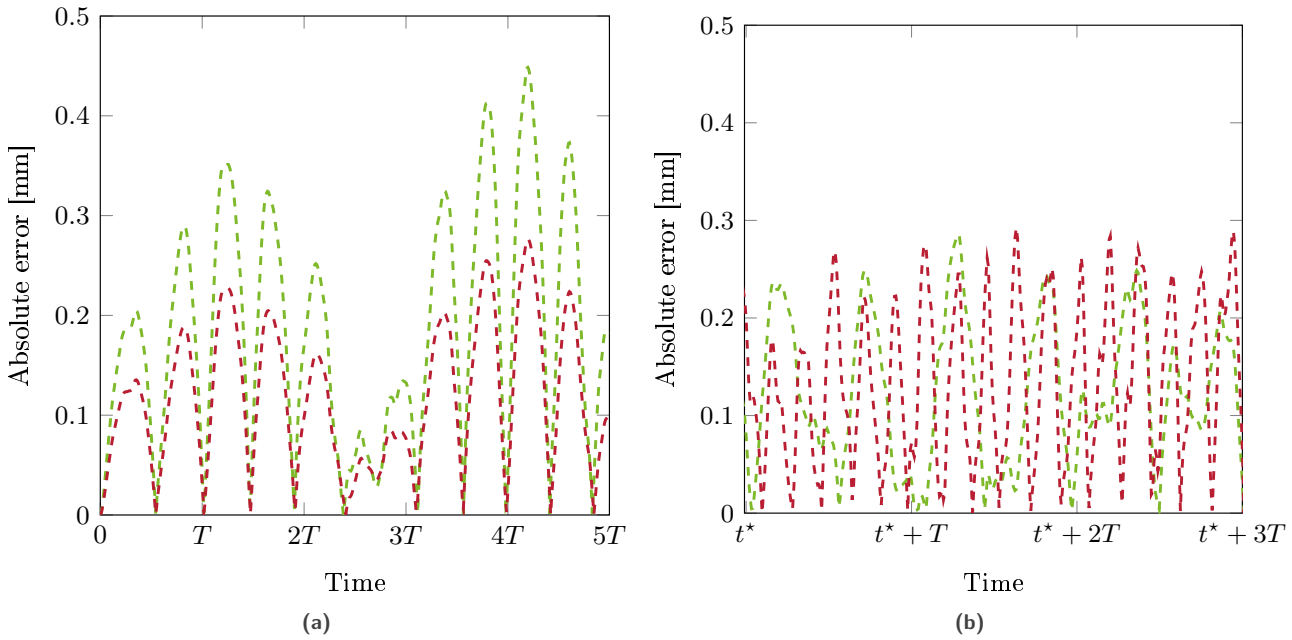

Figure 18. Absolute errors between the nonlinear responses predicted with the full order model and the reduced order models with all modal derivatives (- - -) and with the best 10 modal derivatives according to selection criterion 2b (- - -): (a) transient response and (b) steady-state response.

Fig. 18b. The different reduced models provide very accurate predictions and the initial errors do not build up during the simulation, which underlines the relevance of the proposed selection criterion.

3.3.2 Accuracy of the reduction method

In this section, the performance indicator is used to assess the accuracy of the reduction method and the influence of the number of modal derivatives included in the reduction basis. Reduction bases characterized by $r_b = 3$, $r_c = 10$, $r_{\text{cyclic}} = 144$ and r_{MD} between 2 and 30 are built. The value of r_c has been fixed based on convergence analyses on linear and nonlinear simulations. Increasing r_c beyond this value does not increase the accuracy of the results on the studied frequency range. The same training excitation as in section 3.3.1 is considered, *i.e.* a harmonic excitation in the $\mathbf{e}_z$ direction characterized by $A_t = 400$ N, $\omega_t = 4,000$ rad/s, $N_t = 1$. Figure 19 shows the weights associated to each modal derivative (according to selection criterion 2b) and the ranking of the first 30 modal derivatives. The modal derivative with the highest weight is the derivative of the second static mode with respect to itself, the modal derivative with the second highest weight is the derivative of the second static mode with respect to the third static mode, and so on. More generally, the modal derivatives included in the reduction basis correspond to the derivatives of the static modes with respect to themselves and of the static modes with respect to the first internal modes.

The different reduced order models are first used to compute the response of the bladed disk to harmonic excitations characterized by $A_e = 400$ N, $\omega_e = 4,000$ rad/s, $N_d = 0$ and distributed on respectively $N_e = 1$, 4 and 8 blade tip nodes. Although the training excitation is limited to a single period, the external excitation is here extended to ten periods in order to assess the capability of the reduced order models to accurately predict nonlinear transient phenomena. Results are provided in Fig. 20. The results highlight that the reduced order modeling technique allows predicting the dynamic behavior of the bladed disk for the three values of N_e as the performance indicator eventually reaches values above 0.95 in the three cases. However, the accuracy of the reduced order model decreases as N_e increases and increasing the number of modal derivatives beyond 30 does not seem to improve the performance. The results could be improved by selecting boundary nodes closer to the actual excited nodes. In order to have a more versatile reduced order model, it is interesting to select boundary nodes distributed on the whole

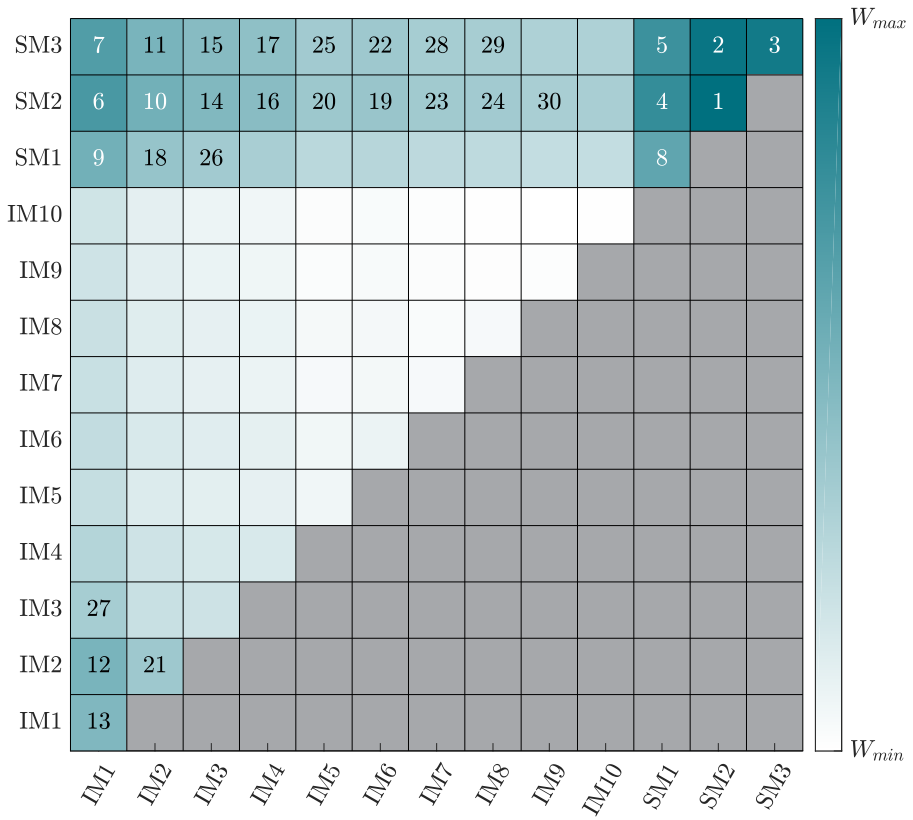

Figure 19. Weights $W_{ij}^{(2b)}$ associated to each modal derivative and their ranking.

blade-tip surface. However, as shown in section 2.3, increasing the number of static modes also leads to a significant increase of the size of the reduction basis as more modal derivatives have to be included in the reduction basis.

The reduced order models are then used to compute the response of the bladed disk to harmonic excitations characterized by $A_e = 400$ N, $N_e = 1$, $N_d = 0$ at different pulsations ω_e. Results are provided in Fig. 21. Results at $\omega_e = 4,000$ rad/s have already been presented in Fig. 20. At this pulsation, the structure mainly responds in the blade first mode and the reduced order models with at least $r_{\mathrm{MD}} = 10$ modal derivatives predict with accuracy the dynamic response.

When the pulsation of the excitation is increased to $\omega_e = 13,000$ rad/s, nearly the same level of accuracy is achieved when a high number of modal derivatives is considered but the convergence is slower. 22 modal derivatives are required to reach a performance indicator I greater than 0.95. In fact, at this pulsation, the second blade mode is also excited (see Fig. 15) and it is necessary to include the modal derivatives related to this torsion mode in the reduction basis. Figure 19 shows that the modal derivative of the second internal mode with respect to itself is included in position 21 in the reduction basis. Given the results in Fig. 21, this modal derivative seems particularly important to represent the dynamics of the structure at this pulsation.

The same conclusions hold at the pulsation $\omega_e = 17,000$ rad/s where the third blade mode is slightly excited. As this pulsation, a disk-dominated mode is also excited. Provided the adequate modal derivatives are included in the reduction basis, the methodology is still accurate to describe the structure dynamics.

It is worth reminding that the modal derivatives selection criterion is based on a training excitation, here defined at a pulsation $\omega_e = 4,000$ rad/s that mainly excites the first mode of the structure. Faster convergence of the results

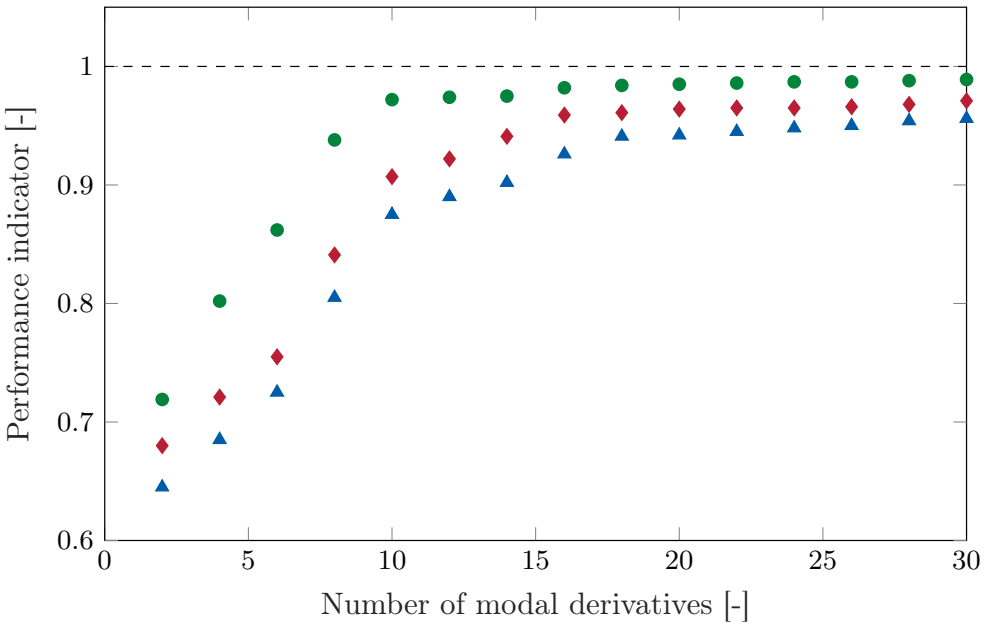

Figure 20. Evolution of the performance indicator as a function of the number of modal derivatives r_{MD} for external excitations characterized by $A_e = 400$ N, $\omega_e = 4,000$ rad/s , $N_d = 0$ and $N_e = 1$ (●), $N_e = 4$ (♦) and $N_e = 8$ (▲).

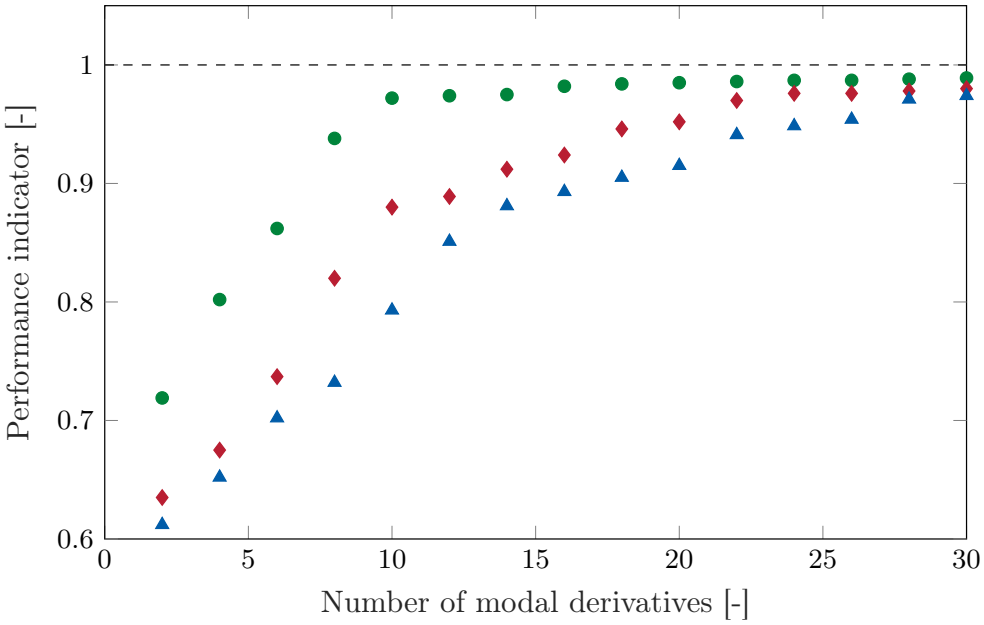

Figure 21. Evolution of the performance indicator as a function of the number of modal derivatives r_{MD} for external excitations characterized by $A_e = 400$ N, $N_e = 1$, $N_d = 0$ and $\omega_e = 4,000$ rad/s (●), $\omega_e = 13,000$ rad/s (♦) and $\omega_e = 17,000$ rad/s (▲).

(in terms of number of modal derivatives) could be reached by modifying the pulsation of this training excitation. Depending on the application and if the frequency range of application of the reduced order model is *a priori* known, it could be relevant to adjust the training excitation characteristics.

Lastly, the reduced order models are used to compute the response of the structure at the three pulsations

studied before but with harmonic excitations characterized by $N_d = 9$ nodal diameters. The results are illustrated in Fig. 22. The tendency of the three curves is very similar to what has been observed in Fig. 21. The reduced order models are also accurate to study excitations with a number of nodal diameters different from 0.

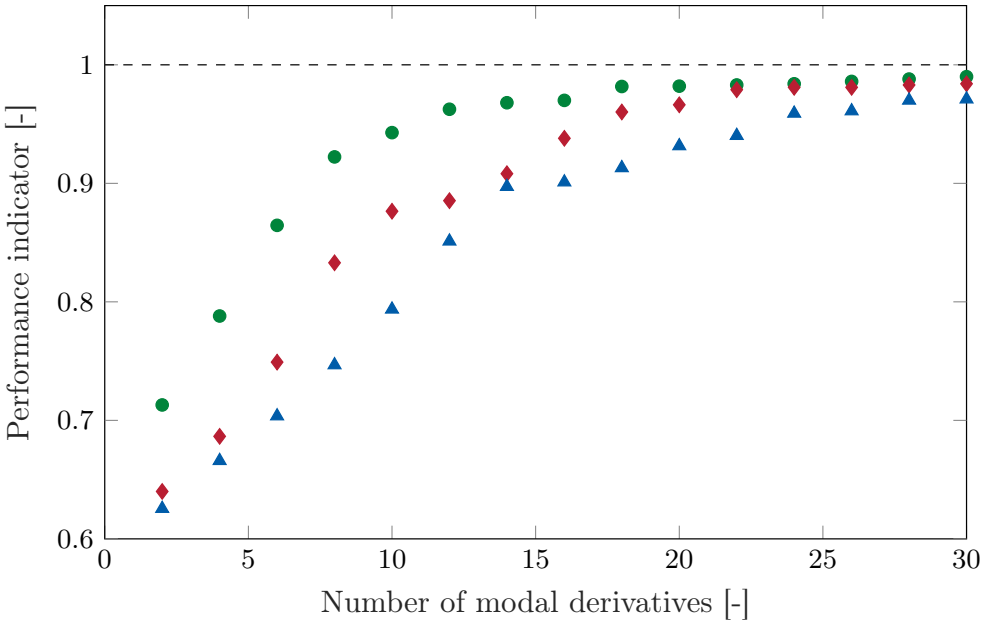

Figure 22. Evolution of the performance indicator as a function of the number of modal derivatives r_{MD} for external excitations characterized by $A_e = 400$ N, $N_e = 1$, $N_d = 9$ and $\omega_e = 4,000$ rad/s (●), $\omega_e = 13,000$ rad/s (♦) and $\omega_e = 17,000$ rad/s (▲).

Also, the level of accuracy at pulsation $\omega_e = 17,000$ rad/s is close to the one obtained for $N_d = 0$ where a disk-dominated mode was also excited. This confirms that such modes do not give rise to any particular issue in the methodology.

Other studies (whose results are not shown here for the sake of conciseness) have been performed with other excitation cases. In particular, these studies showed that the reduced order models are still accurate when the amplitude of the external excitation varies between 100 N and 1000 N, provided enough modal derivatives are included in the reduction basis.

3.3.3 Computational cost

As one of the main objectives of the numerical strategy is to accelerate the simulations, this section provides some information on the computation cost of the procedure. The different computation times presented in the following correspond to single CPU sequential times on an Intel Xeon E5-2698 v4 processor (2.2 GHz). The core numerical tool is written in Python. Full order simulations are performed with the module Mecano of the finite element analysis software SAMCEF [58].

The reduction procedure differentiates between an expensive offline stage where the reduced order model is built and an efficient online stage where the reduced order model is used in simulations. The offline stage is performed once for a given reduction basis, while the online stage can be performed several times, to study different excitation conditions.

Considering a reduction basis of size $r = 972$ ($r_b = 3$, $r_c = 10$, $r_{\text{MD}} = 10$, $r_{\text{cyclic}} = 144$), the time required to build the reduced order model, *i.e.* the offline time, is approximately 10 hours. Note that parallel computing can be used to reduce computation times as the nonlinear force static evaluations of the STEP can be done in parallel to build the tensors $\tilde{\mathbf{A}}^n$ and $\tilde{\mathbf{B}}^n$ for each sector.

The online time, *i.e.* the time required to integrate forward in time the equation of motion, is directly related to the size of the reduction basis, r. With the reduced order model built above ($r = 972$), a dynamic simulation of

length 50 ms (approximately 30 periods at 4000 rad/s) with a time step of integration $h = 10^{-5}$ s takes about 1 minute. By comparison, the same simulation with the full order finite element modes would take about 18 hours. The use of the reduced order model therefore allows a significant reduction of a factor 1000.

3.4 Contact simulations

The methodology is then applied to bladed structures with geometric and contact nonlinearities. Based on the analyses performed on a single rotating blade, a reduced order model with $r_b = 24$ boundary degrees-of-freedom per sector, $r_c = 15$ internal modes per sector, $r_{\text{MD}} = 150$ modal derivatives per sector and $r_{\text{cyclic}} = 144$ is built. This leads to a reduction basis of size $r = 6,948$. The time required to build the reduced order model, *i.e.* the offline time, is approximately 3,000 hours in the same conditions as in section 3.3.3. This reduced order model is used to perform the contact simulations. Convergence studies confirm that the size of the reduced order model is appropriate.

3.4.1 Interaction maps

Simulations at constant angular speed Ω between 1,200 rad/s and 1,650 rad/s are performed (with a step of 5 rad/s). The interaction maps are built as described in section 2.3.1. The interaction maps corresponding to the radial displacement at the node LE of one sector (sector 1) are shown in Fig. 23 in the cases where geometric nonlinearities are neglected and when they are taken into account. With the numerical strategy described in section 2.1.4, building the complete interaction map with geometric nonlinearities takes approximately 400 hours on 20 cores.

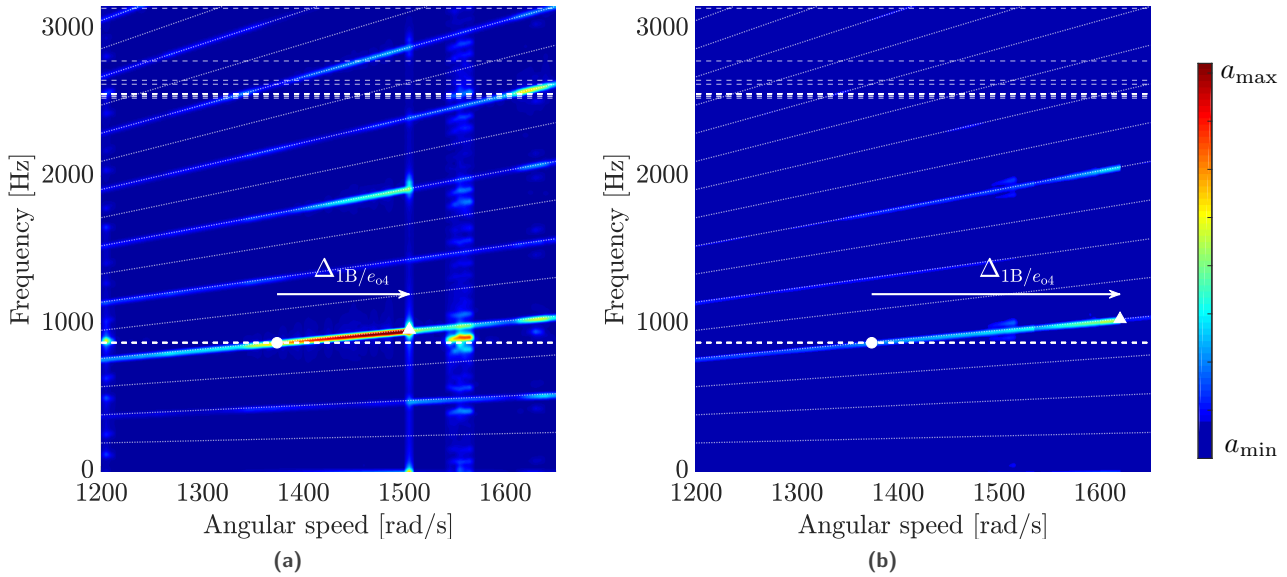

Figure 23. Interaction maps of the radial displacement at node LE with eigenfrequencies (- - -), engine order lines (·····), predicted linear resonance (●) and predicted nonlinear resonance (▲): (a) without geometric nonlinearities and (b) with geometric nonlinearities.

The interaction maps highlight the existence of a strong contact interaction between the first mode family of the bladed disk (corresponding to the first bending mode of the blade) and the fourth engine order. The contact stiffening is indicated by an arrow in both maps. Again, geometric nonlinearities seem to give rise to smoother interactions and be responsible for an additional contact stiffening.

The radial displacement amplitude at node LE is shown in Fig. 24. This figure confirms the observations made with the interaction maps. In order to correctly quantify the contact stiffening of the structure, a continuation procedure should be used to build the nonlinear frequency response curve (as detailed in section 2.3.3). Given the computer resources available and the cost of such simulations, this has not been done here. Indeed, when building

a NFRC with a continuation procedure, simulations at each angular speed have to be done one after the other with a relatively small angular speed step. The strategy detailed in section 2.1.4 can therefore not be used. It is however expected that the contact stiffening is strongly under-estimated in the case where geometric nonlinearities are neglected.

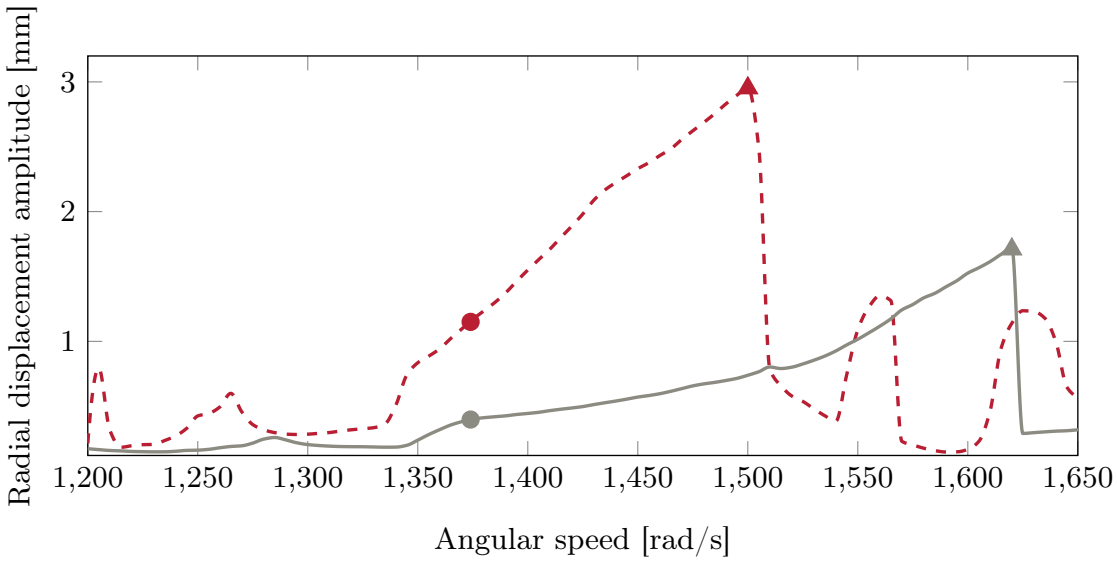

Figure 24. Nonlinear frequency response curve of the radial displacement at node LE in the cases where geometric nonlinearities are not considered (- - -) and where geometric nonlinearities are considered (——) with predicted linear resonance (●) and predicted nonlinear resonance (▲).

3.4.2 Stress analysis

From an industrial point of view, the stress field inside the structure is an important global quantity of interest as it is directly related to the structure integrity. If the maximal stress level exceeds the material yield stress, irreversible deformations may occur, leading eventually to the failure of the structure. The stress fields are here studied at the angular speeds of the nonlinear resonances corresponding to the interaction $1\mathrm{B}/e_{\mathrm{o}4}$ indicated by the symbol (▲) in Fig. 23 and Fig. 24. The von Mises stress fields are computed at time $t_{\max}$ where the node LE of sector 1 reaches its maximal radial displacement. These stress fields in sector 1 are represented in Fig. 25 for the cases where geometric nonlinearities are neglected and where they are taken into account. At time $t_{\max}$, the blade is not subjected to any contact force and is free to oscillate between two bumps.

At these interactions, the response of the structure is dominated by the first bending mode of the blade, which shows slightly different shapes when geometric nonlinearities are considered or not. The zones of maximal von Mises stresses are not located exactly at the same place in both cases. When geometric nonlinearities are neglected, the maximal stresses are found near the root of the blade. When considering the geometric nonlinearities, the zone of maximal stresses is moved toward the center of the blade. Also, the results without geometric nonlinearities highlight non-negligible stresses in the disk. These results suggest that accounting for geometric nonlinearities in bladed disk models could have a significant influence in terms of bladed disks design.

Quantitatively, the ratio of the maximal von Mises stresses in both cases is in line with the corresponding ratio of maximal displacements at the blade tip leading edge. It is important to note that in the case where geometric nonlinearities are neglected, stresses higher than the material yield stress are obtained in the blade while the blade remains in the elastic domain when geometric nonlinearities are taken into account. This confirms that, in the studied case, geometric nonlinearities weaken the interactions, not only locally at the blade tip, but also globally in the whole blade. The analysis of the stress field at the other interaction angular speeds confirms that the severity of the interaction in terms of displacement amplitudes is reflected in the maximal values of the von Mises stress.

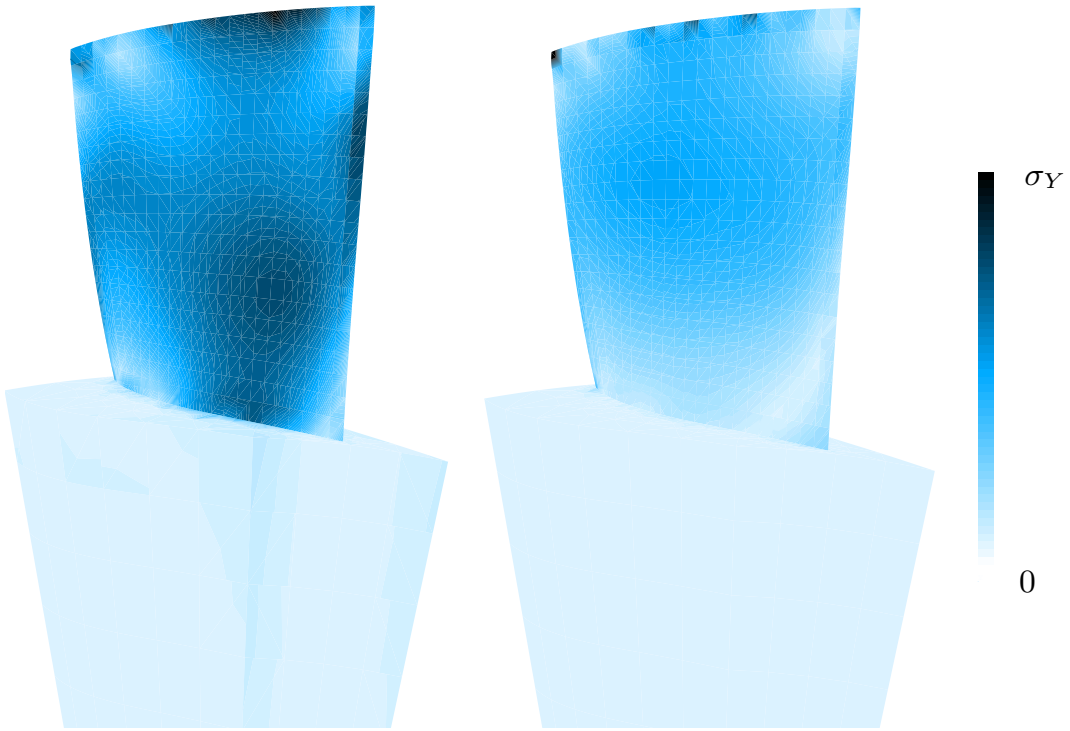

Figure 25. Comparison of the Von Mises stress fields at $t_{\max}$: (a) without geometric nonlinearities and (b) with geometric nonlinearities.

4 Conclusion

This paper is dedicated to the dynamic analysis of bladed structures with geometric nonlinearities subjected to contact interactions. Methodologies based on reduced order modeling techniques are used in order to be numerically efficient.

A recently derived methodology is first used to study the contact dynamics of a single rotating sector. The contact simulations show that geometric nonlinearities have a strong influence on the contact dynamics of blades. In particular, they globally reduce the amplitude of vibration. This is justified by an analysis of the clearance consumption that shows that geometrically nonlinear blades feature a lower clearance consumption, which leads to less strong interactions. Geometric nonlinearities also lead to an additional contact stiffening. However, this contact stiffening has to be carefully quantified. When using a time-integration based methodology, a continuation procedure has to be used to follow the high-amplitude branch of the response and locate correctly the resonance.

The numerical strategy for single-sector structures is then generalized to multi-sector structures by using Component Mode Synthesis. The methodology is validated on a test case subjected to an equivalent aerodynamic loading, without contact interactions. The methodology is then used to study the contact interactions of the full bladed disk. The results show that reduced order models provide an efficient alternative to full order models for the study of the nonlinear dynamics of cyclically periodic structures. The methodology also allows recovering the stress fields in the structure. As the numerical strategy is based on Component Mode Synthesis techniques, mistuning can also easily be included in the reduced order model.

Acknowledgment

E. Delhez is supported by the *Fonds de la Recherche Scientifique* (F.R.S.-FNRS, Belgium) which is gratefully acknowledged. This research was also undertaken thanks to funding from the Canada Research Chairs Program.

References

[1] P. Almeida, C. Gibert, F. Thouverez, X. Leblanc, J.-P. Ousty, Experimental Analysis of Dynamic Interaction Between a Centrifugal Compressor and Its Casing, Journal of Turbomachinery 137 (3) (oct 2014). doi:10.1115/1.4028328.

[2] T. Bui-Thanh, K. Willcox, O. Ghattas, B. van Bloemen Waanders, Goal-oriented, model-constrained optimization for reduction of large-scale systems, Journal of Computational Physics 224 (2) (2007) 880–896. doi:10.1016/J.JCP.2006.10.026.

[3] R. Bladh, Efficient predictions of the vibratory response of mistuned bladed disks by reduced order modeling, Ph.D. thesis, University of Michigan (USA) (2001).
URL https://tel.archives-ouvertes.fr/tel-00358168/

[4] V. Omprakash, V. Ramamurti, Cyclic symmetry approach to the structural dynamic analysis of bladed discs, Communications in Applied Numerical Methods 8 (2) (1992) 81–91. doi:10.1002/cnm.1630080203.

[5] R. Vaidyanathan, S. Santhanam, V. Ramamurti, Static and dynamic analysis of an aerofoil bladed disc using the concept of cyclic symmetry, Communications in Numerical Methods in Engineering 19 (4) (2003) 313–324. doi:10.1002/cnm.571.

[6] R. R. Craig, C.-J. Chang, Free-interface methods of substructure coupling for dynamic analysis, AIAA Journal 14 (11) (1976) 1633–1635. doi:10.2514/3.7264.

[7] P. Seshu, Substructuring and Component Mode Synthesis, Shock and Vibration 4 (3) (1997) 199–210. doi:10.3233/SAV-1997-4306.

[8] R. R. Craig, Coupling of substructures for dynamic analyses: An overview, in: Collection of Technical Papers - AIAA/ASME/ASCE/AHS/ASC Structures, Structural Dynamics and Materials Conference, Vol. 5, AIAA, 2000, pp. 3–14. doi:10.2514/6.2000-1573.

[9] A. Batailly, Simulation de l'interaction rotor/stator pour des turbo-machines aéronautiques en configuration non-accidentelle, Ph.D. thesis, École Centrale de Nantes (France) (2008).
URL https://tel.archives-ouvertes.fr/tel-00364945

[10] S. K. Sinha, Rotordynamic analysis of asymmetric turbofan rotor due to fan blade-loss event with contact-impact rub loads, Journal of Sound and Vibration 332 (9) (2013) 2253–2283. doi:10.1016/j.jsv.2012.11.033.

[11] N. J. Carpenter, R. L. Taylor, M. G. Katona, Lagrange constraints for transient finite element surface contact, International Journal for Numerical Methods in Engineering 32 (1) (1991) 103–128. doi:10.1002/nme.1620320107.

[12] A. Batailly, M. Meingast, M. Legrand, Unilateral contact induced blade/casing vibratory interactions in impellers: Analysis for rigid casings, Journal of Sound and Vibration 337 (2015) 244–262. doi:10.1016/j.jsv.2014.10.010.

[13] A. Grolet, F. Thouverez, Free and forced vibration analysis of a nonlinear system with cyclic symmetry: Application to a simplified model, Journal of Sound and Vibration 331 (12) (2012) 2911–2928. doi:10.1016/j.jsv.2012.02.008.

[14] A. Grolet, Dynamique non-linéaire des structures mécaniques : application aux systèmes à symétrie cyclique, Ph.D. thesis, École Centrale de Lyon (France) (2013).
URL https://tel.archives-ouvertes.fr/tel-01727750

[15] A. Picou, E. Capiez-Lernout, C. Soize, M. Mbaye, Mistuning analysis of a detuned bladed-disk with geometrical nonlinearities, in: Proceedings of the ASME Turbo Expo 2019, Phoenix (USA), 2019. doi:10.1115/GT2019-90820.

[16] A. Picou, Robust analysis under uncertainties of bladed disk vibration with geometrical nonlinearities and detuning, Ph.D. thesis, Université Paris-Est (France) (2019).
URL https://tel.archives-ouvertes.fr/tel-02513425

[17] W. C. Hurty, Dynamic Analysis of Structural Systems Using Component Modes, AIAA Journal 3 (4) (1965). doi:10.2514/3.2947.

[18] R. R. Craig, M. Bampton, Coupling of substructures for dynamic analyses, AIAA Journal 6 (7) (1968) 1313–1319. doi:10.2514/3.4741.

[19] A. Martin, Réduction en dynamique non-linéaire géométrique : Application au cas des structures à symétrie cyclique, Ph.D. thesis, Ecole Centrale de Lyon (France) (2019).
URL https://hal.archives-ouvertes.fr/tel-02476146/

[20] A. Martin, F. Thouverez, Dynamic Analysis and Reduction of a Cyclic Symmetric System Subjected to Geometric Nonlinearities, in: Proceedings of ASME Turbo Expo 2018, ASME, Oslo (Norway), 2018. doi:10.1115/GT2018-75709.

[21] C. Joannin, B. Chouvion, F. Thouverez, J.-P. Ousty, M. Mbaye, A nonlinear component mode synthesis method for the computation of steady-state vibrations in non-conservative systems, Mechanical Systems and Signal Processing 83 (2017) 75–92. doi:10.1016/j.ymssp.2016.05.044.

[22] C. Joannin, F. Thouverez, B. Chouvion, Reduced-order modelling using nonlinear modes and triple nonlinear modal synthesis, Computers & Structures 203 (2018) 18–33. doi:10.1016/j.compstruc.2018.05.005.

[23] E. Capiez-Lernout, C. Soize, M. P. Mignolet, Computational stochastic statics of an uncertain curved structure with geometrical nonlinearity in three-dimensional elasticity, Computational Mechanics 49 (1) (2012) 87–97. doi:10.1007/s00466-011-0629-y.

[24] C. Touzé, M. Vidrascu, D. Chapelle, Direct finite element computation of non-linear modal coupling coefficients for reduced-order shell models, Computational Mechanics 54 (2) (2014) 567–580. doi:10.1007/s00466-014-1006-4.

[25] S. Chaturantabut, D. C. Sorensen, Discrete Empirical Interpolation for Nonlinear Model Reduction, in: Proceedings of the 48th IEEE Conference, Shanghai (China), 2009, pp. 4316–4321. doi:10.1109/CDC.2009.5400045.

[26] A. Muravyov, S. Rizzi, Determination of nonlinear stiffness with application to random vibration of geometrically nonlinear structures, Computers & Structures 81 (15) (2003) 1513–1523. doi:10.1016/S0045-7949(03)00145-7.

[27] M. I. McEwan, J. R. Wright, J. E. Cooper, A. Y. Leung, A combined modal/finite element analysis technique for the dynamic response of a non-linear beam to harmonic excitation, Journal of Sound and Vibration 243 (4) (2001) 601–624. doi:10.1006/jsvi.2000.3434.

[28] E. Delhez, F. Nyssen, J.-C. Golinval, A. Batailly, Reduced order modeling of blades with geometric nonlinearities and contact interactions, Journal of Sound and Vibration 500 (2021). doi:10.1016/j.jsv.2021.116037.

[29] A. Millecamps, J.-F. Brunel, P. Dufrenoy, F. Garcin, M. Nucci, Influence of Thermal Effects During Blade-Casing Contact Experiments, in: Proceedings of ASME 2009 International Design Engineering Technical Conferences & Computers and Information in Engineering Conference (IDETC/CIE 2011), San Diego (USA), 2009. doi:10.1115/DETC2009-86842.

[30] E. Delhez, F. Nyssen, J.-C. Golinval, A. Batailly, Assessment of Geometric Nonlinearities Influence on NASA Rotor 37 Response to Blade Tip/Casing Rubbing Events, Journal of Engineering for Gas Turbines and Power 143 (November) (2021). doi:10.1115/1.4051968.

[31] P. Tiso, Optimal second order reduction basis selection for nonlinear transient analysis, in: Proceedings of the International Modal Analysis Conference (IMAC) XXIX, Jacksonville (USA), 2011, pp. 27–39. doi:10.1007/978-1-4419-9299-4_3.

[32] L. Wu, P. Tiso, F. van Keulen, A modal derivatives enhanced Craig-Bampton method for geometrically nonlinear structural dynamics, in: Proceedings of the 27th International Conference on Noise and Vibration Engineering, Leuven (Belgium), 2016, pp. 3615–3624.

[33] S. R. Idelsohn, A. Cardona, A reduction method for nonlinear structural dynamic analysis, Computer Methods in Applied Mechanics and Engineering 49 (3) (1985) 253–279. doi:10.1016/0045-7825(85)90125-2.

[34] O. Weeger, U. Wever, B. Simeon, On the use of modal derivatives for nonlinear model order reduction, International Journal for Numerical Methods in Engineering 108 (2016) 1579–1602. doi:10.1002/nme.5267.

[35] A. Lazarus, O. Thomas, J. F. Deü, Finite element reduced order models for nonlinear vibrations of piezoelectric layered beams with applications to NEMS, Finite Elements in Analysis and Design 49 (1) (2012) 35–51. doi:10.1016/j.finel.2011.08.019.

[36] A. Givois, A. Grolet, O. Thomas, J. F. Deü, On the frequency response computation of geometrically nonlinear flat structures using reduced-order finite element models, Nonlinear Dynamics 97 (2019) 1747–1781. doi:10.1007/s11071-019-05021-6.

[37] M. Legrand, A. Batailly, B. Magnain, P. Cartraud, C. Pierre, Full three-dimensional investigation of structural contact interactions in turbomachines, Journal of Sound and Vibration 331 (11) (2012) 2578–2601. doi:10.1016/j.jsv.2012.01.017.

[38] A. Batailly, M. Legrand, A. Millecamps, F. Garcin, Numerical-experimental comparison in the simulation of rotor/stator interaction through blade-tip/abradable coating contact, Journal of Engineering for Gas Turbines and Power 134 (8) (2012). doi:10.1115/1.4006446.

[39] A. Batailly, Q. Agrapart, A. Millecamps, J.-F. Brunel, Experimental and numerical simulation of a rotor/stator interaction event localized on a single blade within an industrial high-pressure compressor, Journal of Sound and Vibration 375 (2016) 308–331. doi:10.1016/j.jsv.2016.03.016.

[40] F. G. Van Zee, R. A. van de Geijn, BLIS: A Framework for Rapidly Instantiating BLAS Functionality, ACM Transactions on Mathematical Software 41 (3) (2015). doi:10.1145/2764454.

[41] T. M. Smith, R. van de Geijn, M. Smelyanskiy, J. R. Hammond, F. G. V. Zee, Anatomy of High-Performance Many-Threaded Matrix Multiplication, in: 28th International Parallel and Distributed Processing Symposium, 2014, pp. 1049–1059. doi:10.1109/IPDPS.2014.110.

[42] R. D. Moore, L. Reid, Performance of Single-Stage Axial-Flow Transonic Compressor With Rotor and Stator Aspect Ratios of 1.19 and 1.26, Respectively, and With Design Pressure Ratio of 2.05, Tech. rep., NASA TP 1659 (1980).

[43] L. Reid, R. D. Moore, Design and Overall Performance of Four Highly-Loaded, High Speed Inlet Stages for an Advanced High-Pressure Ratio Core Compressor, Tech. rep., NASA TP 1337 (1978). doi:10.1049/iet-gtd.2015.0403.

[44] J. D. Denton, Lessons from Rotor 37, Journal of Thermal Science 6 (1) (1997). doi:10.1007/s11630-997-0010-9.

[45] E. Piollet, F. Nyssen, A. Batailly, Blade/casing rubbing interactions in aircraft engines: Numerical benchmark and design guidelines based on NASA rotor 37, Journal of Sound and Vibration 460 (2019). doi:10.1016/j.jsv.2019.114878.

[46] E. Delhez, F. Nyssen, J.-C. Golinval, A. Batailly, Comparative study of blades reduced order models with geometrical nonlinearities and contact interfaces, in: Proceedings of ASME Turbo Expo 2020, Virtual (Online), 2020. doi:10.1115/GT2020-14882.

[47] Y. Colaïtis, A. Batailly, The harmonic balance method with arc-length continuation in blade-tip/casing contact problems, Journal of Sound and Vibration 502 (2021). doi:10.1016/j.jsv.2021.116070.

[48] C. D. Monjaraz Tec, J. Gross, M. Krack, A massless boundary component mode synthesis method for elastodynamic contact problems, Computers & Structures 260 (2022) 106698. doi:10.1016/j.compstruc.2021.106698.

[49] D. Hubler, Rotor 37 and stator 37 assembly, Series: Photographs Relating to Agency Activities, Facilities and Personnel, 1973 - 2013 (1977).

[50] A. Batailly, A. Millecamps, Minimising clearance consumption: A key factor for the design of blades robust to rotor/stator interactions?, Proceedings of the ASME Turbo Expo (2016). doi:10.1115/GT2016-56721.

[51] A. Batailly, M. Legrand, A. Millecamps, S. Cochon, F. Garcin, Redesign of a High-Pressure Compressor Blade Accounting for Nonlinear Structural Interactions, Journal of Engineering for Gas Turbines and Power 137 (2) (2014). doi:10.1115/1.4028263.

[52] J. Lainé, E. Piollet, F. Nyssen, A. Batailly, Blackbox optimization for aircraft engine blades with contact interfaces, Journal of Engineering for Gas Turbines and Power 141 (6) (2019). doi:10.1115/1.4042808.

[53] D. Krattiger, L. Wu, M. Zacharczuk, M. Buck, R. J. Kuether, M. S. Allen, P. Tiso, M. R. Brake, Interface reduction for Hurty/Craig-Bampton substructured models: Review and improvements, Mechanical Systems and Signal Processing 114 (2019) 579–603. doi:10.1016/j.ymssp.2018.05.031.

[54] P. Tiso, Effective modal derivatives based reduction method for geometrically nonlinear structures, in: Proceedings of ASME 2011 International Design Engineering Technical Conferences & Computers and Information in Engineering Conference (IDETC/CIE 2011), Washington (USA), 2011, pp. 399–406. doi:10.1115/DETC2011-48315.

[55] S. Jain, P. Tiso, J. B. Rutzmoser, D. J. Rixen, A quadratic manifold for model order reduction of nonlinear structural dynamics, Computers & Structures 188 (2017) 80–94. doi:10.1016/j.compstruc.2017.04.005.

[56] J. B. Rutzmoser, Model Order Reduction for Nonlinear Structural Dynamics Simulation-free Approaches, Ph.D. thesis, Technische Universität München (Germany) (2018).
URL https://link.springer.com/content/pdf/10.1007%2Fs00707-012-0726-9.pdf

[57] P. Apiwattanalunggarn, Modal reduction of nonlinear structural systems using nonlinear normal modes and component mode synthesis, Ph.D. thesis, Michigan State University (USA) (2003).

[58] Siemens, Siemens PLM Software – LMS Samtech Samcef Mecano, Tech. rep. (2014).
URL http://www.plm.automation.siemens.com/de_de/products/lms/samtech/samcef-wind-turbines.shtml#lightview-close